AD-A080 122 NORTHWESTERN UNIV EVANSTON IL DEPT OF CIVIL ENGINEERING F/G 6/5
COMPUTER SIMULATION OF CANOPY-PILOT RESPONSE TO BIRD-STRIKE.(U)
OCT 79 T BELYTSCHKO, E PRIVITZER, W WINDLE F33615-77-C-0529
UNCLASSIFIED AMRL-TR-79-20 NL

1 OF 2
AD
A080122

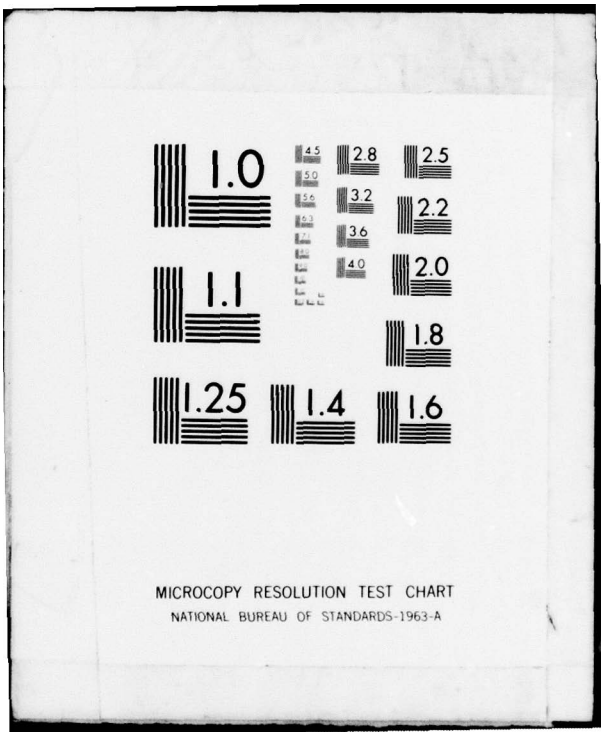
1.0
1.1
1.25
1.4
1.6
1.8
2.0
2.2
2.5
2.8
3.2
3.6
4.0
4.5
5.0
5.6
6.3
MICROCOPY RESOLUTION TEST CHART
NATIONAL BUREAU OF STANDARDS-1963-A

AMRL-TR-79-20

LEVEL II

12

B.S.

COMPUTER SIMULATION OF CANOPY-PILOT RESPONSE TO BIRD-STRIKE

T. BELYTSCHKO
E. PRIVITZER
W. MINDLE
T. WICKS
NORTHWESTERN UNIVERSITY
EVANSTON, ILLINOIS 60201

OCTOBER 1979

AIR FORCE AEROSPACE MEDICAL RESEARCH LABORATORY
AEROSPACE MEDICAL DIVISION
AIR FORCE SYSTEMS COMMAND
WRIGHT-PATTERSON AIR FORCE BASE, OHIO 45433

NOTICES

When US Government drawings, specifications, or other data are used for any purpose other than a definitely related Government procurement operation, the Government thereby incurs no responsibility nor any obligation whatsoever, and the fact that the Government may have formulated, furnished, or in any way supplied the said drawings, specifications, or other data, is not to be regarded by implication or otherwise, as in any manner licensing the holder or any other person or corporation, or conveying any rights or permission to manufacture, use, or sell any patented invention that may in any way be related thereto.

Please do not request copies of this report from Air Force Aerospace Medical Research Laboratory. Additional copies may be purchased from:

National Technical Information Service
5285 Port Royal Road
Springfield, Virginia 22161

Federal Government agencies and their contractors registered with Defense Documentation Center should direct requests for copies of this report to:

Defense Documentation Center
Cameron Station
Alexandria, Virginia 22314

TECHNICAL REVIEW AND APPROVAL

AMRL-TR-79-20

This report has been reviewed by the Office of Public Affairs (PA) and is releasable to the National Technical Information Service (NTIS). At NTIS, it will be available to the general public, including foreign nations.

This technical report has been reviewed and is approved for publication.

FOR THE COMMANDER

HENNING E. VON GIERKE
Director
Biodynamics and Bioengineering Division
Aerospace Medical Research Laboratory

AIR FORCE/56780/6 December 1979 — 150

SECURITY CLASSIFICATION OF THIS PAGE (When Data Entered)

REPORT DOCUMENTATION PAGE

READ INSTRUCTIONS BEFORE COMPLETING FORM

1. REPORT NUMBER: AMRL-TR-79-20	2. GOVT ACCESSION NO.
3. RECIPIENT'S CATALOG NUMBER	
4. TITLE (and Subtitle): COMPUTER SIMULATION OF CANOPY-PILOT RESPONSE TO BIRD-STRIKE	5. TYPE OF REPORT & PERIOD COVERED: Final Technical Report 1 Jun 77 — 15 Sep 78
6. PERFORMING ORG. REPORT NUMBER	
7. AUTHOR(s): T. Belytschko, E. Privitzer, W. Mindle, T. Wicks	8. CONTRACT OR GRANT NUMBER(s): F33615-77-C-0529
9. PERFORMING ORGANIZATION NAME AND ADDRESS: Department of Civil Engineering, Northwestern University, Evanston, Illinois 60201	10. PROGRAM ELEMENT, PROJECT, TASK AREA & WORK UNIT NUMBERS: 62202F; 7231-15-05
11. CONTROLLING OFFICE NAME AND ADDRESS: Air Force Aerospace Medical Research Laboratory, Aerospace Medical Division (AFSC), Wright-Patterson Air Force Base, Ohio 45433	12. REPORT DATE: October 1979 13. NUMBER OF PAGES: 101
14. MONITORING AGENCY NAME & ADDRESS (if different from Controlling Office)	15. SECURITY CLASS. (of this report): UNCLASSIFIED 15a. DECLASSIFICATION/DOWNGRADING SCHEDULE

16. DISTRIBUTION STATEMENT (of this Report)

Approved for public release; distribution unlimited

17. DISTRIBUTION STATEMENT (of the abstract entered in Block 20, if different from Report)

18. SUPPLEMENTARY NOTES

Supported in whole by the AFAMRL Laboratory Director's Fund

19. KEY WORDS (Continue on reverse side if necessary and identify by block number)

Biomechanics
Head
Spine Impact

20. ABSTRACT (Continue on reverse side if necessary and identify by block number)

A computer program was developed for simulating the complete scenario of a bird-strike event: bird-canopy impact, canopy-pilot impact, and the resulting response of the pilot. The response of the pilot was simulated by a previously developed head-spine model, but in order to predict the degree of pilot injury or impairment, a skull brain model based on the maximum strain criterion was incorporated. Additional features which were developed for → [continued over]

DD FORM 1 JAN 73 1473 EDITION OF 1 NOV 65 IS OBSOLETE

SECURITY CLASSIFICATION OF THIS PAGE (When Data Entered)

401 292

these simulations are (1) a plate finite element with the capability of treating geometric nonlinearities due to large deflections and material nonlinearities; (2) a contact-impact algorithm for treating bird-canopy and canopy-helmet impact and (3) a graphical display capability for illustrating the results of simulations.

Simulations were first performed of bird-canopy impacts to determine the mesh refinement necessary to reproduce the magnitudes of experimentally observed deformations and the wave pattern of the observed displacement. It was found that only a very fine mesh proved satisfactory. This mesh could not be used in the computer simulations because of computer core-storage and cost limitations at our computer facility.

Simulations of pilot response to canopy impact showed that the injury potential is quite sensitive to the initial impulse of the bird impact and its location relative to the pilot. A simulation with a 8 cm maximum deflection resulted in a head impact which was definitely tolerable. On the other hand, a 33% increase in this impulse was associated with irreversible injuries.

The addition of these capabilities in the head-spine model should make possible a thorough study of particular features of bird strike, although parameter and scoping studies might be too expensive with the more refined models ($400/simulation). Furthermore, the addition of these features should be useful in the simulation of other crash environments, where they can be used to represent surfaces which impact the pilot.

PREFACE

The research in this final report was performed under Air Force Contract F33615-77-C-0529 awarded to Northwestern University for the period June 1, 1977 to September 15, 1978. The Air Force program monitor was Mr. Ints Kaleps of the Mathematics and Analysis Branch, Biodynamics and Bioengineering Division of the Aerospace Medical Research Laboratory, Aerospace Medical Division of the Air Force Systems Command at Wright Patterson Air Force Base, Ohio. Material parameters and canopy dimensions were provided by Robert C. McCarty of the Air Force Flight Dynamics Laboratory, Wright-Patterson Air Force Base. This study was supported in whole by the Aerospace Medical Research Laboratory Director's Fund.

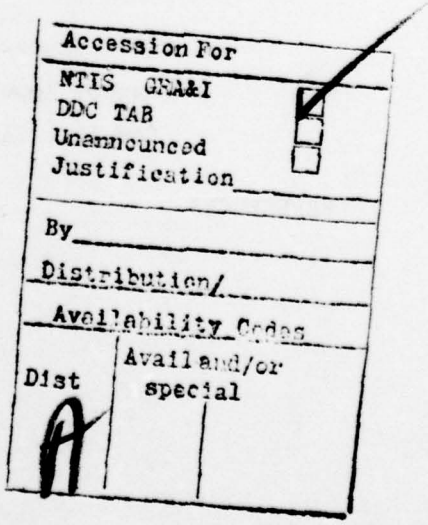

TABLE OF CONTENTS

LIST OF FIGURES

LIST OF TABLES

SECTION 1

INTRODUCTION

Bird impact is a critical problem in the latest production United States Air Force aircraft, the F-16 and the F/FB-111, for its occurrence is not infrequent: 415 incidents were reported in the period 1963-1972 involving the loss of five U.S. planes. In the F-16, bird strike protection is provided by allowing the canopy to deform plastically to absorb the impact energy. However, there is a possibility that the canopy may deform sufficiently to result in contact with the pilot's helmet.

It was the purpose of this study to develop a simulation tool which will enable the designer to simulate bird/canopy impact and any subsequent contact of the canopy with the pilot. In this simulation tool, the pilot is represented by a complete head-spine model including a helmet-head interaction model and a skull-brain model. The severity of the environment and the degree of pilot impairment or injury can be evaluated.

For the purpose of simulating the pilot, the simplified spine model described in Belytschko and Privitzer (1978) AMRL-TR-78-7 was used. In order to permit the evaluation of bird impact in terms of injury and impairment of the pilot, a skull-brain model based on the maximum strain criterion (MSC) of McElhaney, et al (1973) was incorporated in the model. These additional developments, the helmet model, and its interaction with the head are described in Section 3.

The basic simulation tool chosen for the canopy is a large deflection nonlinear finite element code for the transient analysis of plates described by Marchertas and Belytschko (1974), and Belytschko and Marchertas (1974) which was incorporated in the general purpose,

program Structural Analysis of Man (SAM). A contact-impact algorithm was developed for modelling bird-canopy impact and the impact of the canopy with the pilot's helmet. The resulting simulation tool is described in Section 2.

A third development necessary for this project was the coding of appropriate material models for the canopy. The canopy material is nonlinear but it exhibits little permanent deformation. Therefore, a bilinear elastic law, which reproduces the initial stress strain curve of the polyurethane material, but springs back to its initial shape was formulated. This material law and its fit to experimental data are described in Section 4.

Section 5 gives the results of our simulations of bird strike. The initial simulations were performed without a pilot in order to study the effectiveness of the model in reproducing experimental results for canopy deformations. It was found that only a coarse mesh could be used in a complete simulation if core storage and computer cost limitations were to be met, but this mesh was only marginally satisfactory in reproducing observed behavior of the canopy. One simulation of the complete event was made to demonstrate its feasibility, but in the remaining simulations which involved the pilot, the bird impact was represented simply by an impulse at the strike point with a coarse mesh. A computer graphics capability was developed to display the response of the canopy and pilot, and it proved quite valuable in assessing the results.

The simulations show that the injury potential is quite sensitive to the initial impulse, its locations relative to the pilot, and the pilot's location relative to the canopy. One simulation with a 8 cm maximum deflection of the canopy yielded a maximum strain criterion

(MSC) which was certainly tolerable. On the other hand, a 33% increase in the impulse yielded MSC values associated with irreversible injury. These studies were only preliminary, in that certain constants, such as the helmet-head spring constant values were not available while most of the studies were conducted. However, the results indicate that this program, after validation, should provide a valuable tool for the study of bird-canopy impact. Furthermore, the addition of plate elements to the SAM model should be useful in the simulation of crash environments, where they can be used to represent surfaces which impact with the pilot.

SECTION 2

COMPUTATIONAL PROCEDURE

2.1 Definitions and Coordinates

The mathematical model represents the structure by a collection of rigid bodies and deformable elements in a three dimensional space. The format of matrix structural analysis and finite elements is used, so that the topology of the system is quite arbitrary, and complex structures may be modeled.

The deformable elements are interconnected through nodes, as shown in Fig. 2.1.

Two types of nodes are used:

1) primary nodes, each of which has six degrees of freedom consisting of three translations and three rotations; located at the centroids of the rigid bodies;

2) secondary nodes, each of which is connected through a rigid body to a primary node; a secondary node has no independent degrees of freedom.

An arbitrary number of secondary nodes may be associated with any rigid body, and they are used to connect deformable elements to a rigid body at points other than the centroid.

In order to describe the system, we will define three types of coordinate systems:

1) a fixed, global set of coordinates (x,y,z), or x_i;

2) body coordinates $(\bar{x}, \bar{y}, \bar{z})_I$; a triad of unit vectors $\vec{b}_{1I}$, $\vec{b}_{2I}$ and $\vec{b}_{3I}$ are associated with each node I, and $\bar{x}$, $\bar{y}$, and $\bar{z}$ coincide with $\vec{b}_{1I}$, $\vec{b}_{2I}$ and $\vec{b}_{3I}$, respectively. The origin of the $\bar{x}_{iI}$ coordinate system must be at the center of mass.

3) element coordinates $(\hat{x}, \hat{y}, \hat{z})$; a set of element coordinates is associated with each element, and the element coordinates rotate and translate with the element in a manner to be specified later. The $\hat{x}$, $\hat{y}$, and $\hat{z}$ axes are

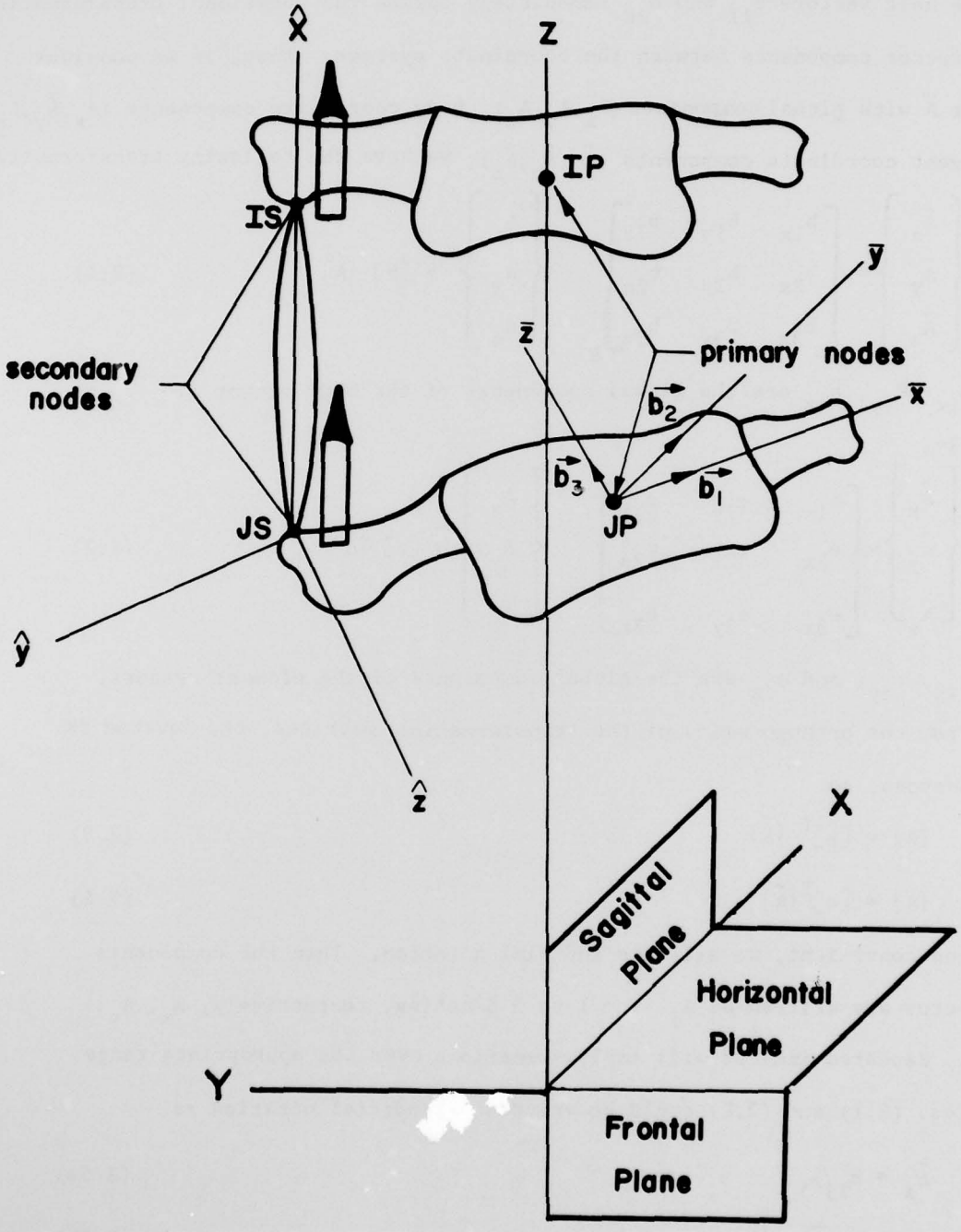

Figure 2.1 Coordinate Systems

associated with unit vectors $\vec{e}_{1E}$, $\vec{e}_{2E}$, and $\vec{e}_{3E}$, respectively, for each element E.

The unit vectors $\vec{b}_{iI}$ and $\vec{e}_{iE}$ immediately define the rotational transformation of any vector components between the coordinate systems. Thus, if we consider a vector $\vec{A}$ with global components (A_x, A_y, A_z), body coordinate components $(\bar{A}_x, \bar{A}_y, \bar{A}_z)$ and element coordinate components $(\hat{A}_x, \hat{A}_y, \hat{A}_z)$, we have the following transformations

$$\begin{Bmatrix} \bar{A}_x \\ \bar{A}_y \\ \bar{A}_z \end{Bmatrix} = \begin{bmatrix} b_{1x} & b_{1y} & b_{1z} \\ b_{2x} & b_{2y} & b_{2z} \\ b_{3x} & b_{3y} & b_{3z} \end{bmatrix}_E \begin{Bmatrix} A_x \\ A_y \\ A_z \end{Bmatrix} = [b]\{A\} \tag{2.1}$$

where b_{ix}, b_{iy}, b_{iz} are the global components of the body vector i.

Similarly,

$$\begin{Bmatrix} \hat{A}_x \\ \hat{A}_y \\ \hat{A}_z \end{Bmatrix} = \begin{bmatrix} e_{1x} & e_{1y} & e_{1z} \\ e_{2x} & e_{2y} & e_{2z} \\ e_{3x} & e_{3y} & e_{3z} \end{bmatrix} \begin{Bmatrix} A_x \\ A_y \\ A_z \end{Bmatrix} = [e]\{A\} \tag{2.2}$$

where e_{ix}, e_{iy}, and e_{iz} are the global components of the element vectors. Also, from the orthogonality of the transformation matrices, the inverse is the transpose, so

$$\{A\} = [b]^T \{\bar{A}\} \tag{2.3}$$

$$\{A\} = [e]^T \{\hat{A}\} \tag{2.4}$$

When convenient, we will use indicial notation. Then the components of a vector are written as A_i, i = 1 to 3 denoting, respectively, A_x, A_y, and A_z. Repeated indices will imply summations over the appropriate range. Thus, Eqs. (2.1) and (2.2) could be written in indicial notation as

$$\bar{A}_i = b_{ij} A_j \tag{2.5a}$$

$$A_i = b_{ji} \bar{A}_j \tag{2.5b}$$

The configuration of the model is described by the positions and orientations of the primary nodes. The original position of node I is denoted

by x^o_{iI} (i=1 to 3 representing the x, y, and z components); the new positions x_{iI} are obtained by adding the displacements u_{iI} to the original position, so

$$x_{iI} = x^o_{iI} + u_{iI} \tag{2.6}$$

The velocities and accelerations of the primary nodes are denoted by $\dot{u}_{iI}$ and $\ddot{u}_{iI}$, respectively.

The orientation of each primary node is described by a triad of orthogonal unit vectors $\vec{b}_{1I}$, $\vec{b}_{2I}$, $\vec{b}_{3I}$, which rotates with the node. The angular velocities and angular accelerations are specified in body coordinate components, $\bar{\omega}_{iI}$ and $\bar{\alpha}_{iI}$, respectively.

The inertial properties of the primary nodes are described by the masses of primary nodes, ρ_I, and the principal moments of inertia of the primary nodes, I_{1I}, I_{2I}, I_{3I}. The nodal vectors $\vec{b}_{iI}$ must coincide with the principal coordinates of the moment of inertia tensor.

The forces and moments at the nodes are denoted by F_{iI} and $\bar{M}_{iI}$, respectively, and may be subdivided into externally applied forces and moments, F^{ext}_{iI} and $\bar{M}^{ext}_{iI}$, and the forces and moments due to the resistance of the deformable elements, F^{int}_{iI} and $\bar{M}^{int}_{iI}$. Moments are always treated in the nodal coordinate systems, $\bar{x}_i$.

The element quantities are extracted from the global quantities in the usual manner of maxtrix structural analysis by a Boolean connectivity matrix $\ell^{(e)}_{AI}$, so that

$$u^{(e)}_{iA} = \ell^{(e)}_{AI}\, u_{iI} \tag{2.7}$$

where

$\ell^{(e)}_{AI}$ = 1 if the Ath generic code of element e corresponds to the Ith primary node of the system.

$\ell^{(e)}_{AI}$ = 0 otherwise

The contributions of the element nodal forces, $\{f^{(e)}\}$ and $\{\bar{m}^{(e)}\}$ to the total nodal forces are obtained by the equation conjugate to Eq. (27)

$$F_{iI}^{int} = \sum_{e} \ell_{AI}^{(e)} f_{iA}^{(e)} \tag{2.8a}$$

$$\bar{M}_{iI}^{int} = \sum_{e} \ell_{AI}^{(e)} \bar{m}_{iA}^{(e)} \tag{2.8b}$$

Since the connectivity matrix is Boolean, the operations of Eqs. (2.7) and (2.8) are never carried out as matrix multiplications. Equation (2.7) simply represents the extraction of a smaller array from larger array, while Eq. (2.8) represents the addition of a smaller array into the appropriate slots of the larger array.

2.2 Equations of Motion

The equations of motion for the system are written separately for the translational and rotational degrees of freedom. The three translational equations are

$$\rho_I u_{iI} = F_{iI}^{ext} - F_{iI}^{int} \quad \text{(no sum on I)} \tag{2.9}$$

Since the $\bar{x}_i$ coordinates are principal coordinates, the rotational equations are

$$\begin{aligned}
I_{1I}\,\bar{\alpha}_{xI} + (I_{3I} - I_{2I})\,\bar{\omega}_{yI}\bar{\omega}_{zI} &= \bar{M}_{xI}^{ext} - \bar{M}_{xI}^{int} \\
I_{2I}\,\bar{\alpha}_{yI} + (I_{1I} - I_{3I})\,\bar{\omega}_{xI}\bar{\omega}_{zI} &= \bar{M}_{yI}^{ext} - \bar{M}_{yI}^{int} \\
I_{3I}\,\bar{\alpha}_{zI} + (I_{2I} - I_{1I})\,\bar{\omega}_{xI}\bar{\omega}_{yI} &= \bar{M}_{zI}^{ext} - \bar{M}_{zI}^{int} \quad \text{(no sum on I)}
\end{aligned} \tag{2.10}$$

On an element basis, the nodal forces and moments are first computed in terms of the corotational element coordinate system $\hat{x}_i$. If an element is connected to a primary node, the nodal forces are then transformed into the global system by

$$\{f^{(e)}\} = [e]^T \{\hat{f}^{(e)}\} \tag{2.11}$$

while the moments are transformed into the nodal coordinate system by

$$\{\bar{m}^{(e)}\} = [b]\,[e]^T\{\hat{m}^{(e)}\} \tag{2.12}$$

The resulting nodal forces are then summed to give the total internal forces and moments.

If an element is connected to a secondary node A which is associated with a primary node I, then it is necessary to account for the rigid linkage in transforming the element nodal forces. We note that the nodal velocities of the secondary node are given by

$$\dot{\bar{u}}_{iA} = \dot{\bar{u}}_{iI} + \Omega_{ij}\,\bar{\omega}_{jI} \tag{2.13}$$

where

$$[\Omega] = \begin{bmatrix} 0 & \bar{z}_{IA} & -\bar{y}_{IA} \\ -\bar{z}_{IA} & 0 & \bar{x}_{IA} \\ \bar{y}_{IA} & -\bar{x}_{IA} & 0 \end{bmatrix} \tag{2.14}$$

where double subscripts designate a difference in node coordinates, e. g.

$$x_{IA} = x_I - x_A \tag{2.15}$$

It can then be shown (Belytschko, et al., (1976)) that the nodal forces at the primary node are given by Eq. (2.11), while the nodal moments are given by

$$\{\bar{m}^{(e)}\} = [b]\,[e]^T\{\hat{m}^{(e)}\} + [\Omega]^T[b]\,[e]^T\{\hat{f}^{(e)}\} \tag{2.16}$$

Thus while for primary nodes the nodal moments are simply related by the coordinate transformations, for secondary nodes, an additional moment is introduced in the transformation because of the moment arm between the nodes.

2.3 Beam Element

The beam element is developed in terms of a corotational formulation as described by Belytschko, et al (1978). In a corotational formulation, displacements and rigid body rotations of each element may be arbitrarily large, but the deformation of each element relative to the corotational

coordinates must be small. This does not limit the formulation to small deformations but imposes the requirement that the number of elements used in the model be sufficiently large so that the deformation of each element relative to its rigid, Cartesian corotational system be small.

Standard engineering beam theory, often known as Euler-Bernoulli beam theory, will be used. This theory assumes that plane sections normal to the midline remain plane and normal. As a consequence, the midline of the beam must rotate with the nodes; if two elements are connected in a straight line, the midline must remain continuous and continuously differentiable. Warping of the beam cross-section will be neglected.

Consider a generic beam element with nodes 1 and 2 as shown in Figure 2.2. The corotational coordinate system $(\hat{x}, \hat{y}, \hat{z})$ for the element is defined by requiring the $\hat{x}$ axis to always pass through the two nodes with its origin at node 1. The $\hat{y}$ axis is defined by the average rigid body rotations about the $\hat{x}$ axis, and the $\hat{z}$ axes is defined by its normality to the $\hat{x}$-$\hat{y}$ plane.

The deformation displacements are then $u_x^{\hat{}def}$, $u_y^{\hat{}def}$, $u_z^{\hat{}def}$, and the rotation $\theta_x^{\hat{}def}$. From the definition of the corotational coordinate system, it follows that $u_x^{\hat{}def}$ vanishes at node 1, while $u_y^{\hat{}def}$ and $u_z^{\hat{}def}$ vanish at both nodes.

The deformation displacement fields are chosen to be polynomials and the lowest order polynomial consistent with Euler-Bernoulli beam theory is used. Since the transverse displacements, $u_y^{\hat{}def}$ and $u_z^{\hat{}def}$, must be continuously differentiable, cubic polynomials are used for these deformation displacements. The axial displacement, $u_x^{\hat{}def}$ and the rotation $\theta_x^{\hat{}def}$

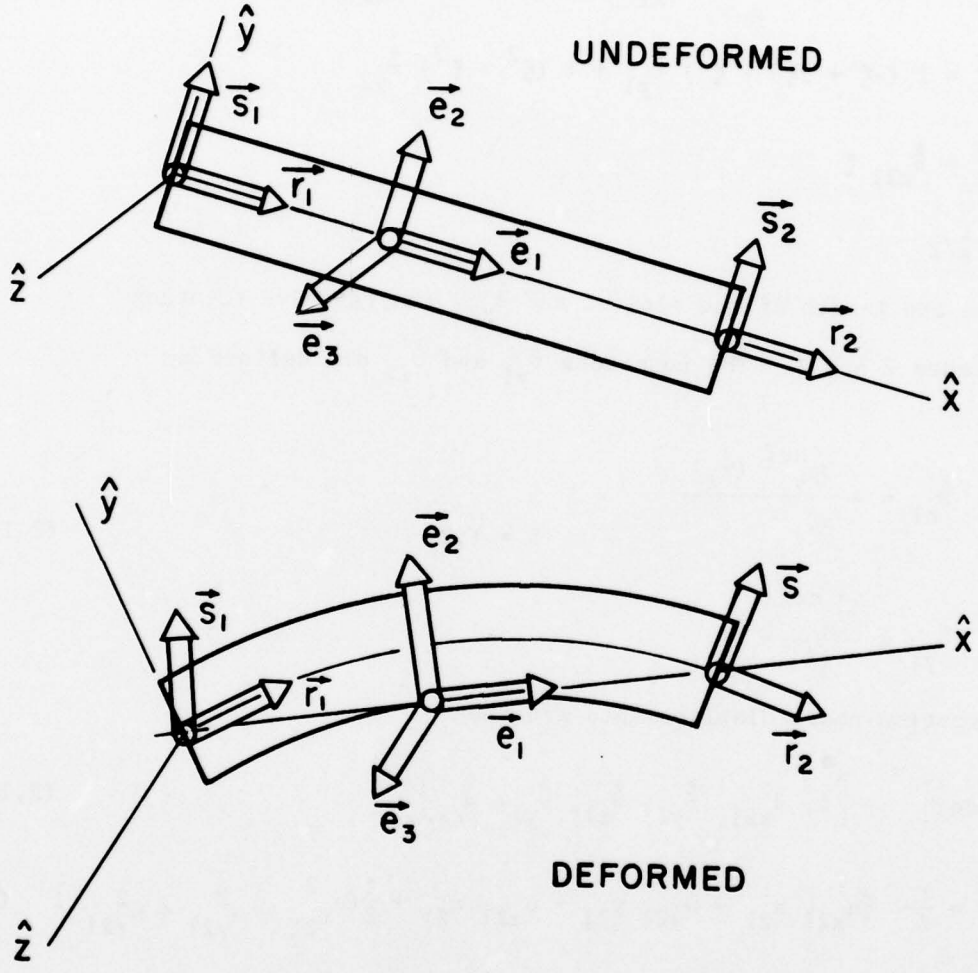

Figure 2.2 Beam Element

need only be continuous, so a linear field is used. Thus,

$$\hat{u}_x^{def} = \hat{u}_{x2}^{def}\,\xi = \delta\xi$$

$$\hat{u}_y^{def} = \ell\,(\xi - 2\xi^2 + \xi^3)\,\hat{\theta}_{z1} + \ell\,(-\xi^2 + \xi^3)\,\hat{\theta}_{z2} \qquad (2.17)$$

$$\hat{u}_z^{def} = \ell\,(-\xi + 2\xi^2 - \xi^3)\,\hat{\theta}_{y1} + \ell\,(\xi^2 - \xi^3)\,\hat{\theta}_{y2}$$

$$\hat{\theta}_x^{def} = \hat{\theta}_{x21}\,\xi$$

$$\xi = \hat{x}/\ell$$

where ℓ is the length of the element and $\hat{\theta}_{x21}$ the relative rotation between nodes 2 and 1. The rotations $\hat{\theta}_{yI}$ and $\hat{\theta}_{zI}$ are defined by

$$\hat{\theta}_{zI} = -\frac{\partial \hat{u}_y^{def}\,(\hat{x}_I)}{\partial \hat{x}} \qquad I = 1,2 \qquad (2.18)$$

$$\hat{\theta}_{yI} = \frac{\partial \hat{u}_z^{def}}{\partial \hat{x}}$$

The deformation nodal displacements are then

$$\left\{\hat{d}^{def}\right\}^T = \left[\delta,\ \hat{\theta}_{x21},\ \hat{\theta}_{y1},\ \hat{\theta}_{z1},\ \hat{\theta}_{yz},\ \hat{\theta}_{z2}\right] \qquad (2.19a)$$

$$\delta = \frac{1}{\ell}\left[u_{x21}\,x_{21} + u_{y21}\,y_{21} + u_{z21}\,z_{21} + \frac{1}{2}(u_{x_{21}}^2 + u_{y21}^2 + u_{z21}^2)\right] \qquad (2.19b)$$

$$x_{21} = x_2 - x_1 \qquad (2.19c)$$

$$u_{x21} = u_{x2} - u_{x1} \qquad (2.19d)$$

where $\delta = \hat{u}_{x2}^{def}$ is the elongation of the beam.

For the purpose of computing $\hat{\theta}_{x21}$, $\hat{\theta}_{yI}$, and $\hat{\theta}_{zI}$ in the deformed

configuration, nodal components of $\vec{e}^{o}_{1I} = \vec{r}_I$ and $\vec{e}^{o}_{2I} = \vec{s}_I$ in the undeformed configuration are stored for both nodes of the element. The nodal (body) components of the vectors $\vec{r}_I$ and $\vec{s}_I$ are considered invariant, so these vectors rotate with the nodes. Consequently, the angle between $\vec{r}$ and $\vec{e}_1$ in the deformed configuration gives the magnitude of rotation of the midline relative to the corotational x-axis of the element; if $\vec{r}$ and $\vec{e}_1$ are coincident in the deformed configuration, the deformation rotations, $\hat{\theta}_y$ and $\hat{\theta}_z$ vanish for the element. For small deformations, the magnitudes of $\hat{\theta}_y$ and $\hat{\theta}_z$ may be found by

$$\hat{\theta}_y \vec{e}_2 + \hat{\theta}_z \vec{e}_3 = \vec{e}_1 \times \vec{r} \tag{2.20}$$

The element components of $\vec{r}$ may be found by Eqs. (2.3) and (2.4) and expressing the right hand side in element coordinates we find

$$\hat{\theta}_y \vec{e}_2 + \hat{\theta}_z \vec{e}_3 = \det \begin{bmatrix} \vec{e}_1 & \vec{e}_2 & \vec{e}_3 \\ 1 & 0 & 0 \\ \hat{r}_x & \hat{r}_y & \hat{r}_z \end{bmatrix} = -\hat{r}_z \vec{e}_2 + \hat{r}_y \vec{e}_3 \tag{2.21}$$

Thus, by equating components, it follows

$$\hat{\theta}_y = -\hat{r}_z \qquad \hat{\theta}_z = \hat{r}_y \tag{2.22}$$

The torsional deformation rotation is found by taking the cross-product of $\vec{s}_1$ with $\vec{s}_2$, and projecting the result on the unit vector along the $\hat{x}$-axis, which gives

$$\hat{\theta}_{x21} = \vec{e}_1 \cdot (\vec{s}_1 \times \vec{s}_2) = \det \begin{bmatrix} \vec{e}_1 & \vec{e}_2 & \vec{e}_3 \\ \hat{s}_{1x} & \hat{s}_{1y} & \hat{s}_{1z} \\ \hat{s}_{2x} & \hat{s}_{2y} & \hat{s}_{2z} \end{bmatrix}$$

$$= \hat{s}_{1y} \hat{s}_{2z} - \hat{s}_{2y} \hat{s}_{1z} \tag{2.23}$$

The strains in a corotational formulation are given by (Belytschko and Hsieh (1973))

$$\hat{\varepsilon}_x = \frac{\partial \hat{u}_x^{def}}{\partial \hat{x}} \tag{2.24}$$

For an Euler-Bernoulli beam, the assumption that normals to the midline remain straight and normal gives

$$\hat{u}_x^{def}(\hat{x}, \hat{y}, \hat{z}) = \hat{u}_x^{def}(\hat{x}, 0, 0) - \hat{y}\frac{\partial \hat{u}_z^{def}}{\partial \hat{x}} - \frac{\partial \hat{u}_y^{def}}{\partial \hat{x}} \tag{2.25}$$

Substituting the above into Eq. (2.24) gives

$$\hat{\varepsilon}_x = \frac{\partial \hat{u}_x^{def}(\hat{x},0,0)}{\partial \hat{x}} - \hat{y}\frac{\partial^2 \hat{u}_z^{def}(\hat{x},0,0)}{\partial \hat{x}^2} - \hat{z}\frac{\partial^2 \hat{u}_y^{def}(\hat{x},0,0)}{\partial \hat{x}^2}$$

For the purpose of determining the shear strains due to torsion, we consider polar coordinates r, θ, in the $\hat{y}$, $\hat{z}$ plane. Then

$$2\hat{\varepsilon}_{r\theta} = \frac{\partial \hat{u}_r^{def}}{\partial \theta} - \frac{\partial \hat{u}_\theta^{def}}{\partial r} \tag{2.26}$$

We assume $\hat{u}_r^{def} = 0$ and that $\hat{u}_\theta^{def}$ varies linearly with r; this assumption is consistent only with cylindrical cross sections. Equations (2.17) and (2.26) and the above assumption, along with our neglect of warping, then gives

$$\hat{\varepsilon}_{r\theta} = \frac{r\theta_{x21}}{\ell} \tag{2.27}$$

Substituting Eq. (2.17) into Eq. (2.25), we then obtain the strain displacement equation for the element to be

$$\begin{Bmatrix} \hat{\varepsilon}_x \\ \hat{\varepsilon}_{r\theta} \end{Bmatrix} = \frac{1}{\ell} \begin{bmatrix} 1 & 0 & \hat{z}(6\xi - 4) & \hat{y}(4 - 6\xi) & \hat{z}(6\xi - 2) & \hat{y}(2 - 6\xi) \\ 0 & r & 0 & 0 & 0 & 0 \end{bmatrix} \begin{Bmatrix} \hat{d}^{def} \end{Bmatrix} \tag{2.28}$$

The above relation defines the strain-displacement matrix [B]. Using the theory of Belytschko and Hsieh (1973), it follows then that the deformation nodal forces are given by

$$\left\{f^{def}\right\} = \int_V [B] \begin{Bmatrix} \hat{\sigma}_x \\ \sigma_{r\theta} \end{Bmatrix} dv \tag{2.29}$$

when V is the volume of the element and where the deformation nodal forces are conjugate to the deformation nodal displacements in the sense that their scalar product gives work, so that

$$\left\{f^{def}\right\}^T = [\hat{f}_{x2}, \hat{m}_{x2}, \hat{m}_{y1}, \hat{m}_{z1}, \hat{m}_{y2}, \hat{m}_{z2}] \tag{2.30}$$

In order to minimize computational expense, it is often desirable to circumvent the volume integration of Eq. (2.29) by defining generalized stresses

$$\hat{m}_x = \int_A r\, \hat{\sigma}_{r\theta}\, dA \tag{2.31a}$$

$$\hat{m}_y = \int_A \hat{z}\, \hat{\sigma}_x\, dA$$

$$\hat{m}_z = -\int_A \hat{y}\, \hat{\sigma}_x\, dA \tag{2.31b}$$

(2.31c)

where A is the cross-sectional area of the beam. The conjugate generalized strains are

$$\hat{\kappa}_y = \frac{\partial^2 \hat{u}_y^{def}}{\partial \hat{x}^2} \tag{2.32a}$$

$$\hat{\kappa}_z = \frac{\partial^2 \hat{u}_z^{def}}{\partial \hat{x}^2} \tag{2.32b}$$

For a linear material, these definitions of generalized stresses and strains may be combined with Eqs. (2.17), (2.29) and (2.31) to yield

$$\begin{Bmatrix} \hat{m}_{y1} \\ \hat{m}_{y2} \end{Bmatrix} = [K_y^b] \begin{Bmatrix} \hat{\theta}_{y1} \\ \hat{\theta}_{y2} \end{Bmatrix} + c_1 [K_y^b] \begin{Bmatrix} \dot{\hat{\theta}}_{y1} \\ \dot{\hat{\theta}}_{y2} \end{Bmatrix} \tag{2.33a}$$

$$\begin{Bmatrix} \hat{m}_{z1} \\ \hat{m}_{z2} \end{Bmatrix} = [K_z^b] \begin{Bmatrix} \theta_{z1} \\ \theta_{z2} \end{Bmatrix} + c_1 [K_z^b] \begin{Bmatrix} \dot{\hat{\theta}}_{z1} \\ \dot{\hat{\theta}}_{z2} \end{Bmatrix} \tag{2.33b}$$

where

$$[K_i^b] = k_i^b \begin{bmatrix} 4+\phi_i & 2-\phi_i \\ 2-\phi_i & 4+\phi_i \end{bmatrix} \tag{2.34a}$$

$$k_i^b = \frac{EI_i}{\ell(1+\phi_i)} \tag{2.34b}$$

where E is Young's modulus, I are the section moduli,

$$I_{yy} = \int_A \hat{z}^2 dA \qquad I_{zz} = \int_A y^2 dA \tag{2.35}$$

and c_1 is a stiffness proportional damping factor. The shear factor ϕ is given by

$$\phi = \frac{24\ (1+\nu)\ I}{A_s\ \ell^2} \tag{2.36}$$

where ν is Poisson's ratio and A_s is the effective area in shear.

While the bending stiffness and torsional stiffnesses have here been expressed in terms of elastic material constants for homogeneous isotropic, elastic beam, in most elements of the biodynamic model, the cross section of the

elements is quite inhomogeneous and anisotropic, and the overall stiffnesses k^a, k^b and k^t; instead the material moduli have been determined experimentally. Therefore, these overall stiffnesses are used directly in the model.

Once the nodal deformation forces are known, the nodal forces required for the equations of motion can be obtained in two steps. First, the remaining six nodal forces (the beam element has two nodes, each with 6 degrees of freedom) are found by equilibrium requirements

$$\begin{aligned}
\hat{f}_{x1} &= -\hat{f}_{x2} & \hat{m}_{x1} &= -\hat{m}_{x2} \\
\hat{f}_{y1} &= \frac{\hat{m}_{z1} + \hat{m}_{z2}}{\ell} & \hat{f}_{y2} &= -\hat{f}_{y1} \\
\hat{f}_{z1} &= -\frac{\hat{m}_{y1} + \hat{m}_{y2}}{\ell} & \hat{f}_{z2} &= -\hat{f}_{z1}
\end{aligned} \tag{2.36}$$

The global components are then found by Eq. (2.3) and (2.4). If the node is a slave node, Eqs. (2.11-13) are used.

2.4 Plate Element

Initially, we considered solving the canopy-pilot interaction problem by using the programs for the pilot, SAM, and the plate finite element program developed at Argonne by Marchertas and Belytschko (1974), SADCAT, interactively. However, we found that considerable core storage would be required to keep both programs in core, while an overlay would involve too much computer time, since the complete simulation involves several hundred time steps, and the two programs would have to be interchanged in fast core for each time step. Both SADCAT and SAM were written in terms of the same nodal updating format and logical structure, so it was decided that the best course would

be to simply incorporate the plate element as another element in the SAM library.

The plate element is a flat, triangular element as shown in Fig. 2.3. Although a curved shell such as a canopy must be approximated as piecewise flat by these elements, past experience (Marchertas and Belytschko (1974)) indicates that it effectively solves curved shell problems. The plate element also uses the corotational formulation. The $(\hat{x}, \hat{y})$ plane is defined to always coincide with the plane defined by the 3 nodes of the element; the origin of the $(\hat{x}, \hat{y})$ coordinate system coincides with node 1, and the $\hat{x}$-axis is aligned so that it bisects the angle between sides $\overline{12}$ and $\overline{13}$; see Fig. 2.2.

The plate element also uses the corotational formulation. The $(\hat{x}, \hat{y})$ plane is defined to always coincide with the plane defined by the 3 nodes of the element; the origin of the $(\hat{x}, \hat{y})$ coordinate system coincides with node 1, and the $\hat{x}$-axis is aligned so that it bisects the angle between sides $\overline{12}$ and $\overline{13}$; see Fig. 2.3.

The deformation displacement field is assumed to be linear in the plane of the element and cubic normal to the plane, and is expressed in terms of the nodal deformation displacements by

$$\begin{Bmatrix} \hat{u}_x^{def} \\ \hat{u}_y^{def} \\ \hat{u}_z^{def} \end{Bmatrix} = \begin{bmatrix} [N_x^m] & [0] \\ [N_y^m] & [0] \\ [0] & [N^f] \end{bmatrix} \begin{Bmatrix} \hat{d}^{def} \end{Bmatrix} \tag{2.37}$$

where $[N^m]$ are the linear triangular shape functions for the membrane (in-plane) displacements (see for example Zienkiewicz (1978)) and $[N^f]$ are the

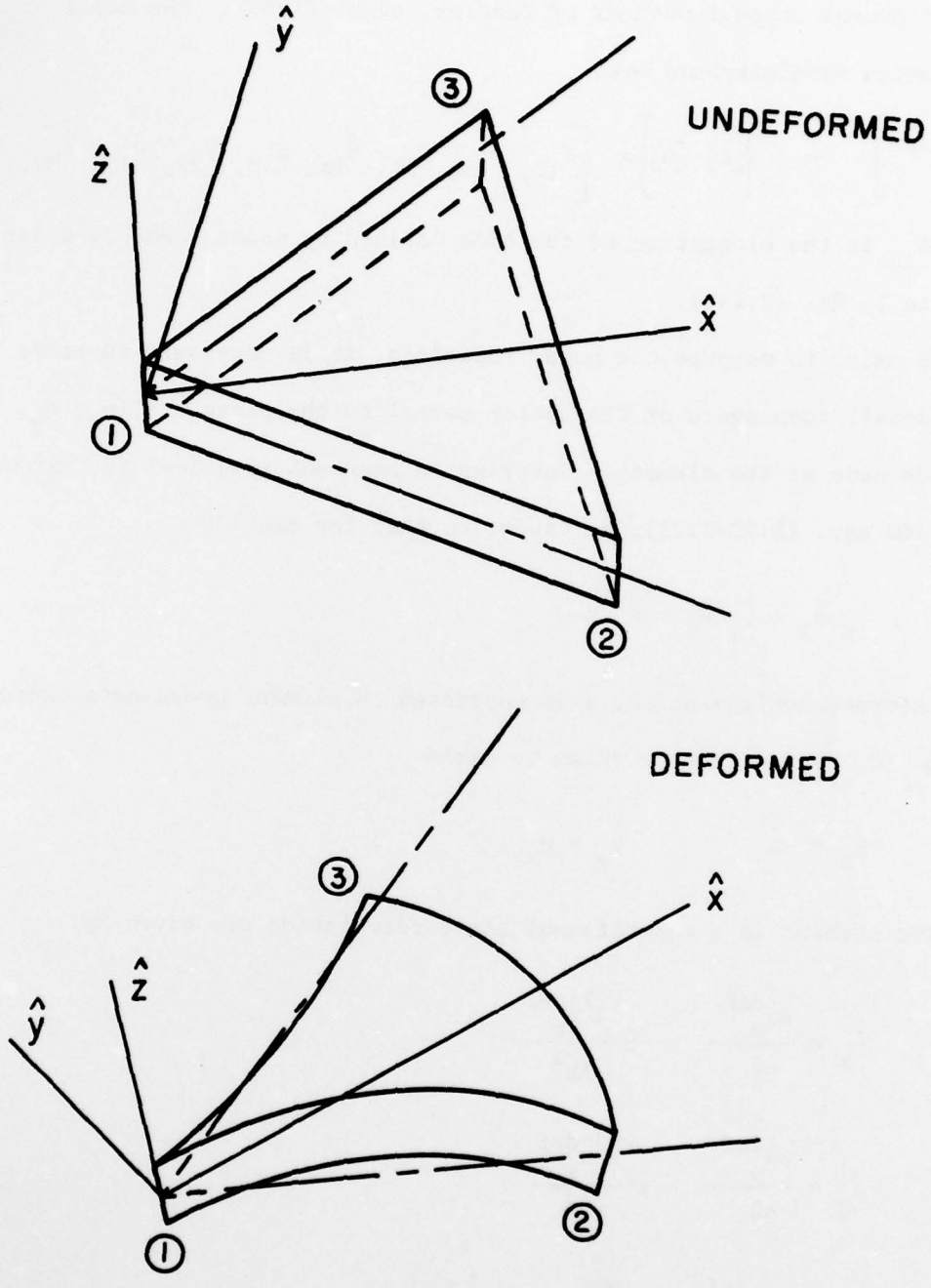

Figure 2.3 Plate Element

cubic flexural shape functions of Bazeley, et al (1965). The nodal deformation displacements are

$$\left\{\hat{d}^{def}\right\}^T = \left\{[\delta]\ [0]\right\} = \left[\delta_{12},\ \delta_{23},\ \delta_{31},\ \hat{\theta}_{1x},\ \hat{\theta}_{1y},\ \hat{\theta}_{2x},\ \hat{\theta}_{2y},\ \hat{\theta}_{3x},\ \hat{\theta}_{3y}\right] \tag{2.38}$$

where δ_{IJ} is the elongation of the side defined by nodes I and J, which is given by Eq. (2.19b).

In order to compute the nodal rotations, it is necessary to store the body (nodal) components of the vector normal to the plate $\vec{n} = (\bar{n}_x, \bar{n}_y, \bar{n}_z)$ for each node of the element. Invoking an argument identical to that used to obtain Eqs. (2.20-2.22), we can write that for small θ

$$\hat{\theta}_x \vec{e}_1 + \hat{\theta}_y \vec{e}_2 = \vec{e}_3 \times \vec{n} \tag{2.39}$$

In a deformed configuration, $\vec{n}$ is expressed in element coordinate-components, and Eq. (2.39) can then be shown to yield

$$\hat{\theta}_x = -\hat{n}_y \qquad \hat{\theta}_y = \hat{n}_x \tag{2.40}$$

The strains in a corotational plate formulation are given by

$$\hat{\varepsilon}_x = \frac{\partial \hat{u}_x^{def}}{\partial \hat{x}} - \hat{z}\,\frac{\partial^2 \hat{u}_z^{def}}{\partial \hat{x}^2} \tag{2.41a}$$

$$\hat{\varepsilon}_y = \frac{\partial \hat{u}_y^{def}}{\partial \hat{y}} - \hat{z}\,\frac{\partial^2 \hat{u}_z^{def}}{\partial \hat{y}^2} \tag{2.41b}$$

$$2\hat{\varepsilon}_{xy} = \frac{\partial \hat{u}_y^{def}}{\partial \hat{x}} + \frac{\partial \hat{u}_x^{def}}{\partial \hat{y}} - 2z\,\frac{\partial^2 \hat{u}_z^{def}}{\partial \hat{x}\,\partial \hat{y}} \tag{2.41c}$$

Inserting Eqs. (2.37) into Eq. (2.41), we obtain

$$\{\hat{\varepsilon}\} = [B^m]\ \{\delta\} - \hat{z}\ [B^f]\ \ \{\hat{\theta}\} \tag{2.42}$$

where

$$\{\hat{\varepsilon}\}^T = [\hat{\varepsilon}_x,\ \hat{\varepsilon}_y,\ 2\hat{\varepsilon}_{xy}] \tag{2.43}$$

$$[B^m] = \begin{bmatrix} \partial N^{\,m}_{xI}/\partial\hat{x} \\ \partial N^{\,m}_{yI}/\partial\hat{y} \\ \partial N^{\,m}_{xI}/\partial\hat{y} + \partial N^{\,m}_{yI}/\partial\hat{x} \end{bmatrix} \tag{2.44}$$

$$[B^f] \quad \begin{bmatrix} \partial^2 N_I{}^f/\partial\hat{x}^2 \\ \partial^2 N_I{}^f/\partial\hat{y}^2 \\ \partial^2 N_I{}^f/\partial\hat{x}\ \partial\hat{y} \end{bmatrix} \tag{2.45}$$

The conjugate nodal deformation forces are separated similarly into membrane forces and moments. The membrane forces are given by

$$\begin{Bmatrix} f_{12} \\ f_{23} \\ f_{13} \end{Bmatrix} = \int_{V_I} [B^m]^T\ \{\hat{\sigma}\}\ dV \tag{2.46}$$

where $\{\hat{\sigma}\}$ is the corotational stress maxtrix

$$\{\hat{\sigma}\}^T = [\hat{\sigma}_x,\ \hat{\sigma}_y,\ \hat{\sigma}_{xy}] \tag{2.47}$$

which is obtained from the strains by the stress-strain law. The nodal deformation moments are given by

$$\{\hat{m}\} = -\int_{V_I} \hat{z}\ [B^f]^T\ \{\hat{\sigma}\}\ dV \tag{2.48}$$

where

$$\{m\}^T = [\hat{m}_{1x}, \hat{m}_{1y}, \hat{m}_{2x}, \hat{m}_{2y}, \hat{m}_{3x}, \hat{m}_{3y}] \tag{2.49}$$

The volume integrals of Eqs. (2.46-48) are evaluated numerically using 3 points in the $(\hat{x}, \hat{y})$ plane, and at each of these points in the plane a variable number of points in the $\hat{z}$ direction (through the depth of the plate element) specified by the user are used for the integration.

The transverse nodal forces $\hat{f}_{zI}$ are then obtained by equilibrium requirements. Moment equilibrium about the $\hat{x}$ and $\hat{y}$ axes gives

$$\begin{Bmatrix} \hat{f}_{2z} \\ \hat{f}_{3z} \end{Bmatrix} = \frac{1}{2A} \begin{bmatrix} \hat{x}_3 & \hat{y}_3 \\ -\hat{x}_2 & -\hat{y}_2 \end{bmatrix} \begin{Bmatrix} \hat{m}_{1x} + \hat{m}_{2x} + \hat{m}_{3x} \\ \hat{m}_{1y} + \hat{m}_{2y} + \hat{m}_{3y} \end{Bmatrix} \tag{2.50}$$

and equilibrium in the $\hat{z}$-direction then gives

$$\hat{f}_{1z} = - \hat{f}_{2z} - \hat{f}_{3z} \tag{2.51}$$

where A is the area of the element. The nodal forces are then transformed into the global coordinates and utilized in the equations of motion as internal nodal forces.

2.5 Time Integration and Stability

In this investigation, time integration was performed by the Newmark β-method with $\beta = 0$, which is an explicit time integration method with stability and convergence properties that are almost identical to the central difference method. The Newmark β-method is sometimes more convenient than the central difference method because all nodal variables and their time derivatives, i.e. velocities and accelerations, are defined at each time step, whereas the central difference method defines velocities only at times equidistant between time steps, often called half-time steps.

In the Newmark β-formulas, the velocities and displacements are

updated in each time step by

$$\dot{u}_{iI}^{j+1} = \dot{u}_{iI}^{j} + \frac{1}{2}\Delta t\,(\ddot{u}_{iI}^{j} + \ddot{u}_{iI}^{j+1})$$

$$u_{iI}^{j+1} = u_{iI}^{j} + \Delta t\,\dot{u}_{iI}^{j} + \frac{1}{2}\Delta t^{2}\,\ddot{u}_{iI}^{j} \tag{2.52}$$

where Δt is the time step and superscript dots denote the time step number.

For the rotational degrees of freedom, Eq. (2.52) cannot be used directly because the orientations are described by the nodal (body) vectors $\vec{b}_{iI}$, and the rates of these vectors are not equivalent to the angular accelerations and velocities.

The counterpart of Eq. (2.52) for the unit vector $\vec{b}$ is

$$\vec{b}_i^{\,j+1} = \vec{b}_i^{\,j} + \Delta t\,\frac{d\vec{b}_i^{\,j}}{dt} + \frac{1}{2}\Delta t^{2}\,\frac{d^{2}\vec{b}_i^{\,j}}{dt^{2}} \tag{2.53}$$

$$\frac{d\vec{b}_i^{\,j+1}}{dt} = \frac{d\vec{b}_i^{\,j}}{dt} + \frac{1}{2}\left(\frac{d^{2}\vec{b}_i^{\,j}}{dt^{2}} + \frac{d^{2}\vec{b}_i^{\,j+1}}{dt^{2}}\right) \tag{2.54}$$

From vector analysis, it follows that

$$\frac{d\vec{b}_i}{dt} = \vec{\omega} \times \vec{b}_i \tag{2.55}$$

$$\frac{d^{2}\vec{b}_i}{dt^{2}} = \vec{\omega} \times (\vec{\omega} \times \vec{b}_i) + (\vec{\alpha} \times \vec{b}_i) \tag{2.56}$$

To obtain the updated components of the unit vectors, we temporarily fix the $\bar{x}_i$ coordinates and consider a particular unit vector; we then dot Eq. (2.53) with the unit vector corresponding to the component of $\vec{b}_i$ to be updated, and substitute Eqs. (2.55) and (2.56) into the resulting expressions. For example, the updated $\bar{x}$-component of $\vec{b}_3$ is found by letting i = 3 in Eq. (2.53) and taking the scalar product with $\vec{b}_1$, which

yields after some simplification to

$$\bar{b}_{3x}^{j+1} = \Delta t\, \bar{\omega}_y^{\,j} + \frac{1}{2}\Delta t^2\, (\bar{\omega}_x^{\,j}\, \bar{\omega}_z^{\,j} + \bar{\alpha}_y^{\,j}) \tag{2.57}$$

Similarly

$$\bar{b}_{3y}^{j+1} = -\Delta t\, \bar{\omega}_x^{\,j} + \frac{1}{2}\Delta t^2\, (\bar{\omega}_y^{\,j}\, \bar{\omega}_z^{\,j} - \bar{\alpha}_x^{\,j}) \tag{2.58a}$$

$$\bar{b}_{1y}^{j+1} = \Delta t\, \bar{\omega}_z^{\,j} + \frac{1}{2}\Delta t^2\, (\bar{\omega}_x^{\,j}\, \bar{\omega}_y^{\,j} + \bar{\alpha}_z^{\,j}) \tag{2.58b}$$

Normality and orthogonality of the unit vectors are used to find the remaining components. It is assumed that the rotations during a time step are small so that second order terms can be neglected. From normality, it follows that

$$b_{3z}^{j+1} = \left[1 - \left(\bar{b}_{3x}^{j+1}\right)^2 - \left(\bar{b}_{3y}^{j+1}\right)^2\right]^{1/2} \tag{2.59}$$

and if we assume that $b_{1x}^{j+1} \sim 1$, orthogonality yields

$$\bar{b}_{1z}^{j+1} = -\left(\bar{b}_{3x}^{j+1} + \bar{b}_{1y}^{j+1}\, \bar{b}_{3y}^{j+1}\right)\, \bar{b}_{3z}^{j+1} \tag{2.60}$$

Finally, the component $\bar{b}_{1x}^{j+1}$ can be found by the normality condition

$$\bar{b}_{1x}^{j+1} = \left[1 - \left(\bar{b}_{1y}^{j+1}\right)^2 - \left(\bar{b}_{1z}^{j+1}\right)^2\right]^{1/2} \tag{2.61}$$

The vector $\vec{b}_2$ is then found by the cross-product.

The components of the $\vec{b}_1$ and $\vec{b}_3$ vectors given above are in terms of the $\bar{x}_i$-coordinates (nodal coordinates) at time step j. These components are then transformed to global components by the transformation (2.3).

In explicit time integration, unless the time step is sufficiently small, numerical instabilities will render the results worthless. Although stability analyses cannot be performed for the fully nonlinear case,

experience indicates that a linearized analysis gives useful estimates of the stable time step. The destabilizing effects of nonlinearities can usually be overcome by reducing the time step that is used by 10% to 20% below the linear stability limit. Although this does not always insure a stable computation, stability can be checked after the computation by examining the energy balance.

A linearized analysis of the Newmark β-method indicates that

$$\Delta t \leq \frac{2}{\omega_{max}} \left[\left(1 + \mu^2 \right)^{1/2} - \mu \right] \tag{2.62}$$

where ω_{max} is the highest frequency of the system and μ is the fraction of critical damping in the highest frequency. The frequency ω corresponds to the maximum eigenvalue of the eigenvalue problem

$$\left[K \right] \left\{ X \right\} = \omega^2 \left[M \right] \left\{ X \right\} \tag{2.63}$$

where [K] is a linear global stiffness matrix and [M] is the mass matrix. This stability limit is obtained by performing a Fourier analysis of the uncoupled equation

$$\ddot{x} + 2 \mu \omega \dot{x} + \omega^2 x = 0 \tag{2.64}$$

No provisions are made in the program for directly computing the maximum eigenvalue ω, for it would require considerable programming and computer time, and it would only be of marginal usefulness in nonlinear problems since [K] and [M] can change dramatically with time. Instead, we have developed formulas for estimating ω. These are based on Rayleigh's theorem, which allows us to bound the maximum frequency of the system by the maximum frequency among all of the elements of the system (see Hughes,

et al (1978)), i.e.

$$\omega_{max} \leq \sup \quad \omega_{max}^{ele} \tag{2.65}$$

where ω_{max}^{ele} is the maximum of the highest frequency of all elements in the system.

The maximum frequency of any of the elements can easily be obtained exactly or approximated sufficiently accurately for our purposes. First we will consider a spring element with a spring constant k^a. The element stiffness $[k]$ and mass $[m]$ matrices are given by

$$[k] = k^a \begin{bmatrix} 1 & -1 \\ -1 & 1 \end{bmatrix} \qquad [m] = \begin{bmatrix} m_1 & 0 \\ 0 & m_2 \end{bmatrix} \tag{2.66}$$

where m_1 and m_2 are the lumped masses at the nodes. The maximum frequency is given by

$$\omega_{max}^2 = \frac{4k^a}{m_1 + m_2} \tag{2.67}$$

Whenever the system consists of a system of springs connecting rigid bodies, all springs in parallel between any two rigid bodies should be summed to obtain the total spring constant between the two rigid bodies. For the purpose of using Eq. (2.67), half of the lumped masses at each of the nodes should be used. While in principle the entire lumped mass could be used, it should be noted that the same mass cannot be ascribed to two elements in estimating the maximum frequency. Therefore, if all of the mass is used in estimating the frequency for any one element, the adjacent elements will have no mass, which will increase the frequency associated with that element.

When the lumped masses arise from the density of the element itself, then

$$m_1 = m_2 = \frac{1}{2} \rho A \ell \tag{2.68}$$

where ρ is the density. If the stiffness is associated with an elastic material with Young's modulus E, then

$$k^a = AE/\ell \tag{2.69}$$

Substituting these values into Eq. (2.67), we find

$$\omega_{max}^2 = \frac{4E}{\rho \ell^2} = \frac{4c^2}{\ell^2} \tag{2.70}$$

or

$$\omega_{max} = \frac{2c}{\ell} \tag{2.71}$$

where c, given by

$$c^2 = \frac{E}{\rho}$$

is the wavespeed in the material. Substituting this result with Eq. (2.62), we obtain

$$\Delta t \leq \frac{\ell}{c} \left(\sqrt{\mu^2 + 1} - \mu \right) \tag{2.73}$$

so that when $\mu = 0$, the stability limit on the time step corresponds to the time for the elastic wave to traverse the length of the element.

When an element with flexural stiffness connects two nodes, its effects on stability must be considered separately. For this purpose, it is sufficient to consider bending in one plane. The stiffness matrix (if the shear effect is zero) is then (see Przeminiecki (1968))

$$[k] = \frac{EI}{\ell^2} \begin{bmatrix} 12 & 6\ell & -12 & 6\ell \\ & 4\ell^2 & -6\ell & 2\ell^2 \\ & & 12 & -6\ell \\ \text{symmetric} & & & 4\ell^2 \end{bmatrix} \tag{2.74}$$

and we will consider a mass maxtrix

$$[m] = \frac{\rho A \ell}{420} \begin{bmatrix} 210 & 0 & 0 & 0 \\ & \alpha\ell^2 & 0 & 0 \\ & & 210 & 0 \\ \text{symmetric} & & & \alpha\ell^2 \end{bmatrix} \tag{2.75}$$

The maximum frequency is given as a function of α by the roots of the equation

$$\alpha^2(\mu^2 - 0.115\mu) + \alpha(0.229 - 8\mu) + 12 = 0$$
$$\mu = \frac{\rho A \ell^4 \omega^2}{420EI} \tag{2.76}$$

For $\alpha = 17.5$, which is the lumping we use whenever the mass arises from the density distribution of the element itself, the solution is

$$\omega_{max}^2 = \frac{192\, c^2 I}{A\ell^4} \tag{2.77}$$

For a typical model, it is possible that either the frequency associated with axial response, Eq. (2.67), or flexural frequency, Eq. (2.77), is the largest. In choosing the time step, it is the <u>largest</u> frequency which must be used. In comparing Eq. (2.71) and (2.77), it can be seen that the axial frequencies increase inversely with ℓ, whereas the flexural frequencies increase inversely as ℓ^2. Hence, for sufficiently refined models, the flexural frequency will govern the time step.

The frequency associated with a torsional mode is given by

$$\omega_{max}^2 = \frac{4k^t}{\bar{I}_{x1} + \bar{I}_{x2}} \tag{2.78}$$

This frequency should also be checked, but it is generally smaller than the axial frequencies.

For the plate element, membrane frequencies can be estimated by Eq. (2.71) with ℓ the smallest distance in the element from a node to the opposite side. Equation (2.77) is used in the form

$$\omega_{max}^2 = \frac{16\, c^2 h^2}{\ell^4} \tag{2.79}$$

where h is the thickness of the plate; ℓ is used in the same sense as for the membrane frequencies.

The relation between stiffness proportional damping c, in Eq. (2.33) and μ is given by

$$\mu = \frac{c_1}{\omega_{max}} \tag{2.80}$$

If artificial viscosity is used, the artificial viscosity constant corresponds with μ. The formulas for stability calculations are summarized in Table 2.1.

To insure post facto that the computations are stable, energy balance checks were made as follows: The kinetic energy at each time step j is defined by

$$T^j = \frac{1}{2}\, \rho_I\, (u_{iI}^j)^2 + \frac{1}{2}\, I_{iI}\, (\omega_{iI}^j)^2 \tag{2.81}$$

where I is summed over the primary nodes in the system. The external work is defined by a trapezoidal integration in time, so

$$W^{ext,o} = 0 \tag{2.82}$$

$$W^{ext,j} = W^{ext,j-1} + \frac{1}{2}\, (u_{iI}^j - u_{iI}^{j-1})\, (F_{iI}^{ext,j} + F_{iI}^{ext,j-1})$$

Table 2.1

Guidelines for Stable
Time Step in Explicit Calculations

$$\Delta t = \frac{2}{\omega_{max}} \left[\sqrt{1 + \mu^2} - \mu\right]$$

	Square of Frequency ω_{max}^2
Spring + lumped masses	$\frac{4k}{m_1 + m_2}$
Spring uniform mass	$\frac{4c^2}{\ell^2}$
Beam uniform mass	$\frac{4c^2}{\ell^2}$ or $\frac{192c^2 I}{A\ell^4}$
Plate	Same as beam with ℓ = shortest distance from node to opposite edge

The internal work is similarly defined by

$$W^{int,o} = 0 \tag{2.03}$$

$$W^{int,j} = W^{int,j-1} + \frac{1}{2} (\hat{u}^{(e),j}_{iA} - \hat{u}^{(e),j-1}_{iA}) (\hat{f}^{(e),j}_{iA} + \hat{f}^{(e),j-1}_{iA})$$

Energy balance then requires that

$$W^{int,j} + T^{j} - W^{ext,j} < \epsilon(W^{int,j} + T^{j}) \tag{2.84}$$

If ϵ is greater than about 0.05, a solution is considered unacceptable. The source of the energy error may be an arrested or incipient numerical instability, or excessive truncation error.

2.6 Contact-Impact Formulation

Explicit time integrations are easily modified to handle the contact, impact, and subsequent release of two bodies when a diagonal, lumped mass matrix is used. The original continuum then becomes a collection of particles (masses) with interacting forces (springs). This collection may then be analyzed by assuming that linear momentum is conserved during collision and modifying the computed accelerations and velocities appropriately.

We will first discuss the fundamental assumptions made in our impact formulation. This done, we will then detail the flow and basic operation of the subroutine which implements this formulation.

The following assumptions are made:

1. Linear momentum is conserved during impact.
2. The actual impact is smeared over the time step Δt and is plastic.
3. The time step Δt is small enough so that contact may take place with only one element during that time.

4. The time step Δt is small enough so that any wave propagated by the impact only reaches nodes directly adjoining the contact elements; this is guaranteed in an explicit integration by the Courant stability conditions.
5. Internal (spring) forces remain constant during impact.
6. The time step Δt is small enough so that the deformed configuration before impact is the same after impact.
7. The motion of an adjoining node of two elements contacted during a time step is equivalent to a weighted average of one body contacting it.
8. Thermal energy of impact is dissipated completely into the environment surrounding the bodies.
9. All sliding is frictionless.
10. Rigid body rotation of the pilot's head during the time step impact is negligible when compared to the translational velocities.
11. The plate elements are treated as flat, triangular surfaces.

The first assumption is a fundamental axiom in dynamics, the second is a smoothing approximation with the view that as $\Delta t \rightarrow 0$ the response approaches a suitable solution. The third through fifth assumptions permit a total uncoupling of the system during impact and allow one to work with a single element, and the sixth is introduced to avoid any iteration in determining the "true" impact point (see Hughes (1975) for a treatment of this). The error this approximation induces is small and has been found to have little effect on the results. The seventh assumption is needed to prevent any iteration in the impact

analysis. It is felt that such an iteration would be very harmful to computing efficiency. The eighth is made since the constitutive model of the canopy does not incorporate any temperature softening or temperature melting law and since there is no capability for a heat transfer analysis at present in the program. The last assumptions are made for the sake of smoothness and simplicity of programming.

We will now describe the algorithm which implements contact-impact. We define here as master nodes the canopy nodes, slave nodes the nodes of the bird or helmet. Impact is defined the first time step during which contact between two bodies is detected.

1. Update all nodal displacements without considering the possibility of contact.
2. Check for contact between different bodies. If there is no penetration or contact, then continue to the next time step.
3. If contact between a bird and the canopy has taken place, determine the elements contacted by each node of the bird and interpolate the mass of the bird to the adjoining nodes of the element. Then adjust the component of the displacement of the bird normal to the canopy, so that it lies in the plane of the plate element and satisfies any boundary conditions. If contact takes place between the pilot's helmet and the canopy; adjust the vertical displacement of the head so that only one point of the helmet lies on the surface of the plate element, and interpolate the mass of the helmet to the nodes of the contact element.

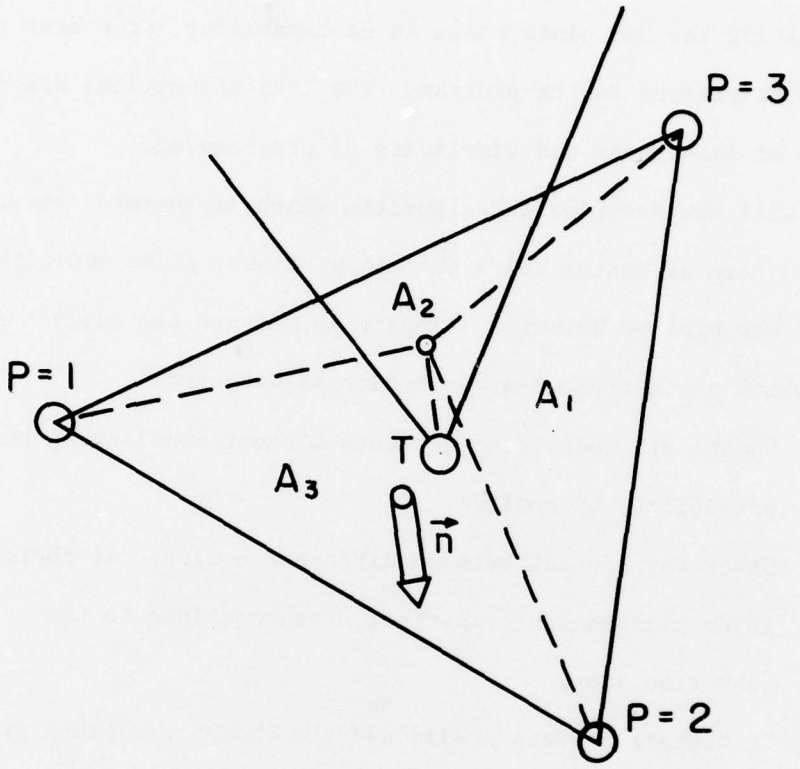

Figure 2.4 Illustration of Contact-Impact

4. In the case of impact, use conservation of momentum and the notion of plastic impact to modify the normal velocities of master nodes. For both impact and continuing contact, modify the normal accelerations to reflect the kinematic coupling.
5. Obtain the new slave node velocities and accelerations by interpolation on the element surface.

The equations used are as follows. To check for contact between a node T and an element e with nodes P = 1, 2, 3, one first needs to check the normal distance between node T and element e. Observing Figure 2.4, we see that this amounts to calculating,

$$B = (\vec{x}_T - \vec{x}_P) \cdot \vec{n} \tag{2.85}$$

where $\vec{n}$ is the "inward" normal of the element and $\vec{x}_T$ and $\vec{x}_P$ are the coordinates of nodes T and P; B is the distance the nodes has penetrated element e, so if $B \geq 0$ the node T may have penetrated element e.

In order to insure penetration has occurred for element e instead of another element, we compute the projected areas using the vector cross-product

$$A_p = \frac{1}{2} \left| (\vec{x}_{P+1} - \vec{x}_{P+2}) \times (\vec{x}_T - \vec{x}_{P+2}) \cdot \vec{n} \right| \tag{2.86}$$

Here P + 1 denotes the node on the counterclockwise side of P in element e. Then if $B \geq 0$ for any P and $0 \leq A_p \leq A = \sum_{p=1}^{3} A_p$, contact has taken place during the time step with element e.

If contact or penetration has taken place, the new position of the

bird node is determined by

$$\vec{x}_T^{+} = \vec{x}_T - B\,\vec{n} \tag{2.87}$$

The superscript (+) denotes the time immediately after contact.

A slightly different procedure for locating the new position of the contact node must be followed when node T has to satisfy boundary conditions, such as on lines of symmetry. Let us assume, for example, that nodes 1 and 2 of the plate element lie in the $x_1 - x_2$ plane which is a line of symmetry. If we followed the previous procedure for calculating $\vec{x}_T^{+}$ we would incorrectly move $\vec{x}_T$ out of the x^1-x^2 plane, because the plate element is not necessarily normal to the line of symmetry. Therefore, we let $\vec{n} = (n_1, n_2, 0)$ and use Eq. (2.87) with this normal vector.

We may use a similar procedure for computing the new position when the pilot's helmet and the canopy impact. The helmet is a sphere of radius R, but its primary node is at its center. The condition for contact or penetration then becomes

$$B \geq R \tag{2.88}$$

with the same conditions on A_p. Eq. (2.87) is similarly replaced by

$$\vec{x}_T^{+} = \vec{x}_T - (B - R)\,\vec{n} \tag{2.89}$$

The point of contact, $\vec{x}_c$, is

$$\vec{x}_c^{+} = \vec{x}_T^{+} - R\vec{n} \tag{2.90}$$

Once contact is established with a plate element, the plate element nodes become the master nodes in driving the normal component of the

displacements. For this purpose, it is necessary to ascribe the nodal masses of the slave nodes, i.e. the bird or head, to the master nodes. If the mass of node T is denoted ρ_T, the mass of node T is given after contact by

$$\rho_P^+ = \rho_P + \rho_T \, A_p/A \tag{2.91}$$

To obtain the velocity at each node, we note that only the normal direction is influenced by impact in the absence of friction. The normal component of any vector is given by

$$\dot{u}_n = \dot{u}_i \, n_i \tag{2.92}$$

The modifications which simulate impact are then as follows:

$$\dot{u}_{Pn}^+ = \frac{\rho_P \dot{u}_{Pn} + \rho_T \, \dot{u}_{Tn}}{\rho_P^+} \tag{2.93a}$$

$$\ddot{u}_{Pn} = \frac{\rho_P \, \ddot{u}_{Pn} + \rho_T \, \ddot{u}_{Tn}}{\rho_P^+} \tag{2.93b}$$

The velocities and accelerations are then interpolated to the birds positions so that only the normal direction is coupled we need. For this purpose, only the linear part of the shape functions are used, which gives

$$\dot{u}_{Tn}^+ = \frac{1}{A} \sum_{I=1}^{3} A_P \, \dot{u}_{Pn}^+ \tag{2.94}$$

$$\ddot{u}_{Tn}^+ = \frac{1}{A} \sum_{I=1}^{3} A_P \, \ddot{u}_{Pn}^T$$

The tangential velocities are uneffected by impact since friction is neglected.

In time steps subsequent to impact (continuing contact), Eqs. (2.93a) and (2.94a) are not used; instead the normal velocities are simply updated using the integration formulas, Eqs. (2.52).

SECTION 3

PILOT MODEL AND INJURY CRITERION

3.1 Spine Model

For the purpose of representing the pilot, the simplified spinal model (SSM) described by Belytschko and Privitzer (AMRL/TR-78-7) is used. The more complex models described in that report, such as the complex spine model (CSM) and the isolated ligamentous spine with viscera (ILSV), which were developed in Belytschko et al (1976) were not used because:

1. Details of lower spine response are not of interest, so any model which represents the overall flexural and axial response of the spine is adequate.

2. The computational cost and computer storage required by the SSM are considerably less than for the other two models, which proved of advantage since a considerable number of degrees of freedom are required to model a canopy.

In the original SSM, the thoracolumbar spine is modelled by three beam elements, T1-T10, T10-L3, and L3-S1, as shown in Fig. 3.1. The longitudinal actions of the viscera are modelled with four spring elements and three masses between the pelvis and T10. The interaction between the viscera and the spine is modelled with a spring element at each visceral mass. However, the neck portion of the model, which was modelled in the original SSM model by a single beam element, has been refined by subdividing the single beam into three beam elements; this allows the mass of the neck to be more uniformly distributed

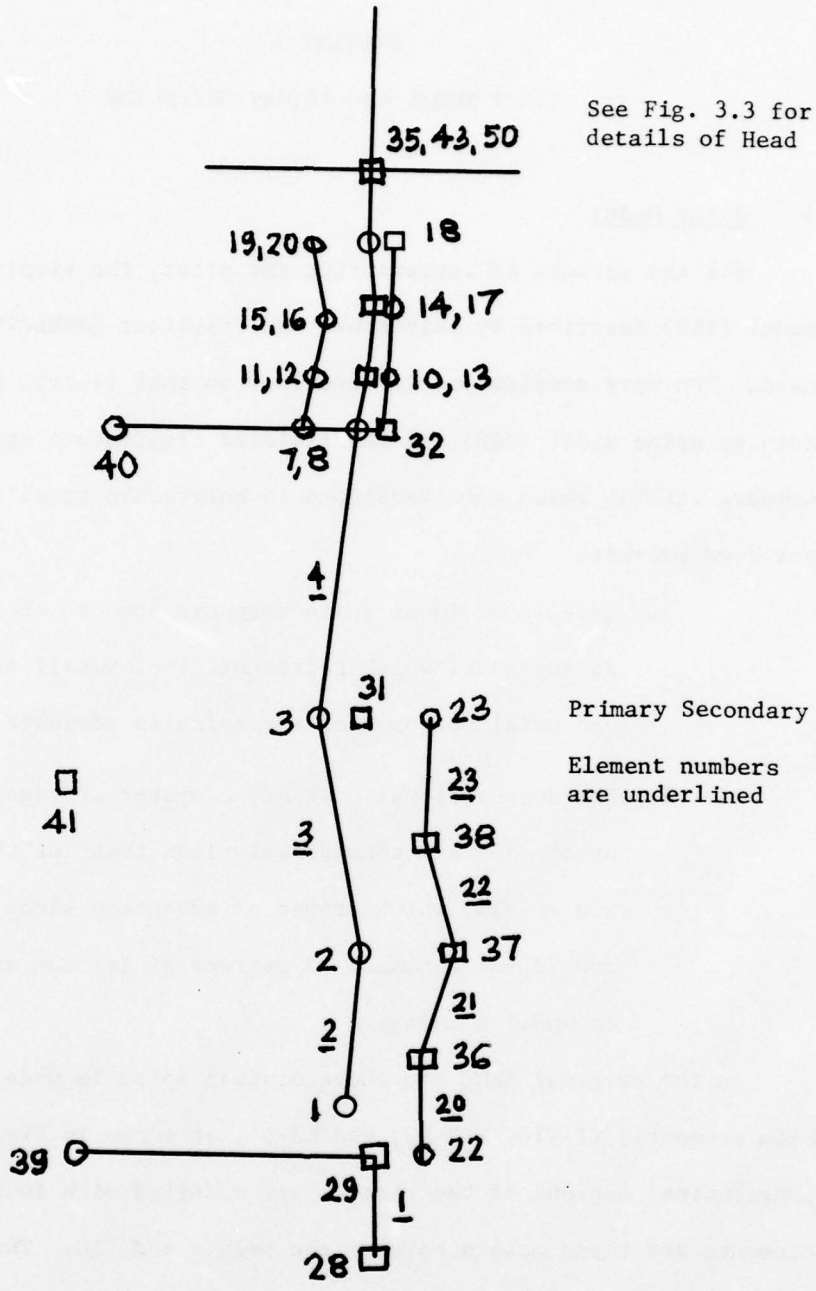

Figure 3.1 Nodes and Elements in Simplified Spine Model (SSM)

between C7 and T1. Refinement of the neck is considered of importance in this study since its response plays a significant role in head impact.

The nodal mass distribution and stiffness properties of the elements of SSM are given in Tables 3.1 and 3.2, respectively. Both the masses and stiffnesses were obtained from the more complex models by combining the masses and using appropriate series formulas for the stiffnesses. The stiffnesses of the individual vertebral motion segments were originally developed by Schultz, et al (1973), while the visceral stiffnesses were obtained by Belytschko and Privitzer (1978) by matching impedance data. The inertial data is based on Liu and Wickstrom (1973).

Although the simplified spine model, unlike the isolated ligamentous spine model or the complex spine model, does not represent the individual vertebrae, it was felt desirable to have the ALFA PLOT graphical display procedures developed for the other spine models also available for the simplified spine model. This was accomplished by developing a short post-processing routine for the program SAM, which linearly interpolates the unit vectors, $\vec{b}_i$ and the positions u_{iI} for each of the vertebral bodies which does not correspond to a node in the SSM. An illustration of the resulting graphical display may be found in Figure 3.2.

III.2 Head and Injury Model

Available injury models may be classified as follows:

1. Simple severity indices based on the magnitude and duration of the acceleration time history.
2. Indices based on responses of single degree of freedom models which represent the skull-brain impedance.

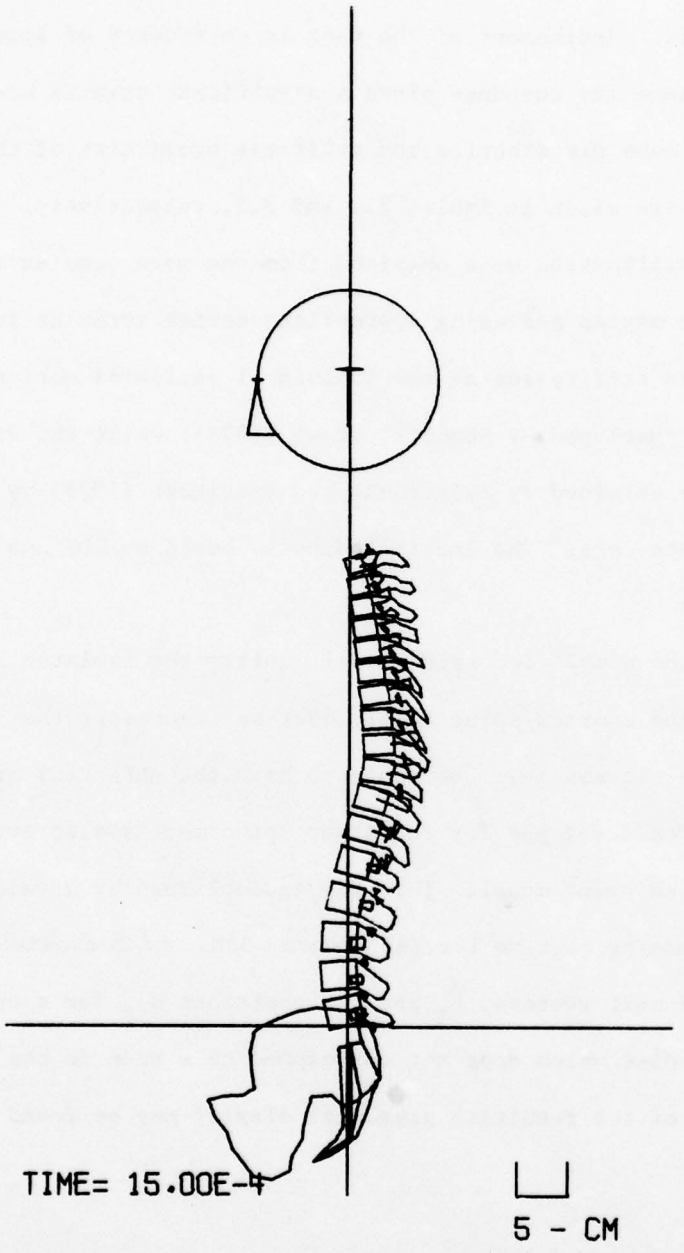

Figure 3.2 Computer Graphics Display of Simplified Spine Model (SSM)

Table 3.1

Stiffness Data for
Simplified Spine Model

Element number	Approximate Physical Region	Stiffnesses		
		Axial k^a dynes	Bending 1 & 2 k_1^b & k_2^b dyne-cm	Torsional k^t dyne-cm
2	S L3-S1	5.68E + 8	3.43E + 8	3.5E + 8
3	S T10-L3	3.47E + 8	2.15E + 8	1.87E + 8
4	S T1-T10	1.54E + 8	6.67E + 7	4.86E + 7
5	S C6-C7	4.32E + 8	2.07E + 9	1.55E + 8
6	S C3-C5	"	"	"
7	S C2-C4	"	"	"
20	Viscera	5.4E + 6		
21	"	8.26E + 6		
22	"	1.03E + 7		
23	"	8.75E + 6		
24	Viscera	5.0E + 6		
25	Spine	5.0E + 6		
27	Interconnectors	1.0E + 7		
28		1.0E + 7		

Table 3.2

Mass Data for Simplified Spine Model

Primary Node Number I	Approximate Physical Region	Mass gm ρ_I	Moments of inertia gm - cm^2 I_{1I}	I_{2I}	I_{3I}
28	Seat	-	-	-	-
29	Pelvis	2.940E + 4	1.308E + 6	2.029E + 6	1.938E + 6
30	S L3-L5	1.660E + 3	3.996E + 4	5.786E + 4	2.800E + 4
31	S+V T6-L2	6.846E + 3	5.328E + 5	8.560E + 5	8.307E + 5
32	T C6-T5	5.896E + 3	2.835E + 5	6.625E + 5	7.429E + 5
33	T C4-C5	6.654E + 2	1.428E + 4	2.410E + 4	3.861E + 4
34	T C1-C3	6.374E + 2	1.421E + 4	1.263E + 4	2.106E + 4
35	Brain	3.940E + 3	1.420E + 5	1.420E + 5	1.420E + 5
36	V L4-L5	4.295E + 3	1.272E + 5	2.985E + 5	3.158E + 5
37	V L2-L3	3.368E + 3	1.203E + 5	3.484E + 5	3.746E + 5
38	V T10-L1	5.134E + 3	2.576E + 5	5.598E + 5	6.257E + 5
41	Seatback	-	-	-	-
43	Skull	6.570E + 2	3.790E + 4	3.790E + 4	3.790E + 4
50	Helmet	1.400E + 3	1.000E + 5	1.000E + 5	1.000E + 5

V = Viscera

S = Spine

T = Torso or neck

3. Continuum models of the skull-brain system which are solved either by analytic or finite element methods.

We will review the applicability and appropriateness of various models for this study, beginning with the last category. Analytical continuum models of the head have been quite numerous and are reviewed by Y. K. Liu (1978) and by Engin and Engin (1975). Although these models have brought about some understanding of the phenomological aspects of head injury in impact environments, they have not been successfully correlated with injury. Recent finite element models of the head and brain seem to be substantially more successful, in that correlations have been obtained between injury and predicted maximum intercranial pressure (Ward (1978)). However, these models are so complex that their incorporation in a bird simulation, where the canopy, head and spine must be simultaneously modeled, would entail exorbitant computational resources.

For these reasons, our attention was restricted to injury models in the first and second categories. In the first category, the most well known are the Wayne State Tolerance Curve (WSTC), Lissner (1960), the Gadd Severity Index (GSI), and the Head Injury Criterion (HIC) proposed by J. Versace (1971) and then modified by NHTSA. In the WSTC, the injury potential is based simply on the average acceleration and its duration. A curve relating the threshold average acceleration to the pulse duration is given; below this curve, at most cerebral concussions without aftereffects are predicted.

In the GSI, the injury potential is expressed in terms of the

acceleration history $a(t)$ and duration τ by

$$GSI = \int_c^{\tau_2} a^n (t)\, dt \tag{3.1}$$

where n is a weight factor, with the recommended value of 2.5. A GSI value of 1,000 is considered life threatening. The HIC is a modification of the GSI in which the following formula is used

$$HIC = t_{21}\left(\frac{1}{t_{21}} \int_{t_1}^{t_2} a\, dt\right)^n \tag{3.2}$$

where t_1 and $t_{21} = t_2 - t_1$ are chosen as to maximize the HIC. This criterion has been normalized against injury data so that an HIC threshold for life threatening injury is 1,000.

The second category of injury indices are based on single degree of freedom models of the skull-brain, which can be described by the equation

$$\ddot{z} + 2\beta\, \Omega\, \dot{z} + \Omega^2\, z = 0 \tag{3.3}$$

where z represents a relative displacement or an effective strain for the system, Ω is a period for the system usually based on impedance data, and β the fraction of critical damping. Several models of this type have been introduced by the Vienna Institute. In the work of A. Slattenscheck (1968), a natural angular frequency of 634 radians per second and a critical damping coefficient of 1.0 is used. Injury potential is based on the maximum value of z, as compared to a tolerance, thus leading to a J index defined by:

$$J = \frac{z_{max}}{z_t} \tag{3.4}$$

where z_t equals to 0.092 inches. The threshold value for J for human tolerance is 1.0. Subsequent models of this type have been based on

revised values of Ω, β and z_t. The latest model reported in an NHSTA (1969) report uses a natural frequency of 175 radians per second, a fraction of critical damping of 0.4 and a z_t value of 1.25 inches.

Stalnaker, et al (1971), McElhaney, et al (1973) have revised these models and performed extensive correlations to injury data. This model has come to be known as the maximum strain criterion (MSC) model for the injury potential. Injury is related to the displacement of the one degree of freedom system, which is conceptualized as an average strain in the brain.

In the MSC, experimentally determined head injury data for living primates is used to define a tolerable mean strain for humans. McElhaney et al defined the mean strain as the displacement of one side of the head relative to the other, divided by the distance across the cranium. Using experimental data they report that their preliminary mean strain level of 0.0061 may be used as an injury criterion in modeling human head impact, and called this a tolerable mean strain, which is the mean "strain corresponding to accelerations required to produce an ESI (Estimated Severity of Injury) of level class 3, moderate but reversible type of injury."

Put simply, the MSC states that an element strain (for the elements representing the interaction of the brain and the skull) less than 0.0061 indicates at most moderate but reversible injury levels, while an element strain greater than 0.0061 indicates non-reversible and possibly fatal injury levels. A strain value of 0.00329 was established by Stalnaker, et al as a survivable acceleration pulse.

McElhaney, et al compared their MSC injury criterion with other head impact injury criteria - the GSI (Gadd Severity Index), the HIC

(Head Injury Criterion), the JTI (Vienna Institute Index), the EDI (Effective Displacement Index), and the RBM (Revised Brain Model). They give brief descriptions of these criteria, and present the results of a study which demonstrates that the MSC, EDI, RBM and JTI predict essentially the same injury levels, while the HIC and GSI predict somewhat higher injury levels.

Because of the computational simplicity and extensive correlation with injury data available for the MSC, it was chosen for use in this model. We will now describe the way in which this head injury model was incorporated in the biodynamic model.

Figure 3.3 depicts the lateral and top views of the head model. This model consists of three concentric spheres, which are interconnected by springs, and represent the brain, skull and helmet, respectively. This model was incorporated into the Simplified Spine Model (SSM). Although it is a rather simple head model, it allows for the direct application of the Mean Strain Criterion (MSC).

The spring constants and masses for this model are based partially on mechanical impedance results for the head presented by McElhaney, et al. The dominant peak for both lateral and anterior-posterior motion was reported to be in the vicinity of 300 Hz (1.88×10^3 rad/sec). It is assumed that this is the natural frequency of the brain/skull system. The natural circular frequency of a two mass-spring system is given by

$$\Omega^2 = \frac{(m_1 + m_2)\ 2k}{m_1\ m_2} \tag{3.5}$$

where m_1 and m_2 are the masses and k is an effective spring constant.

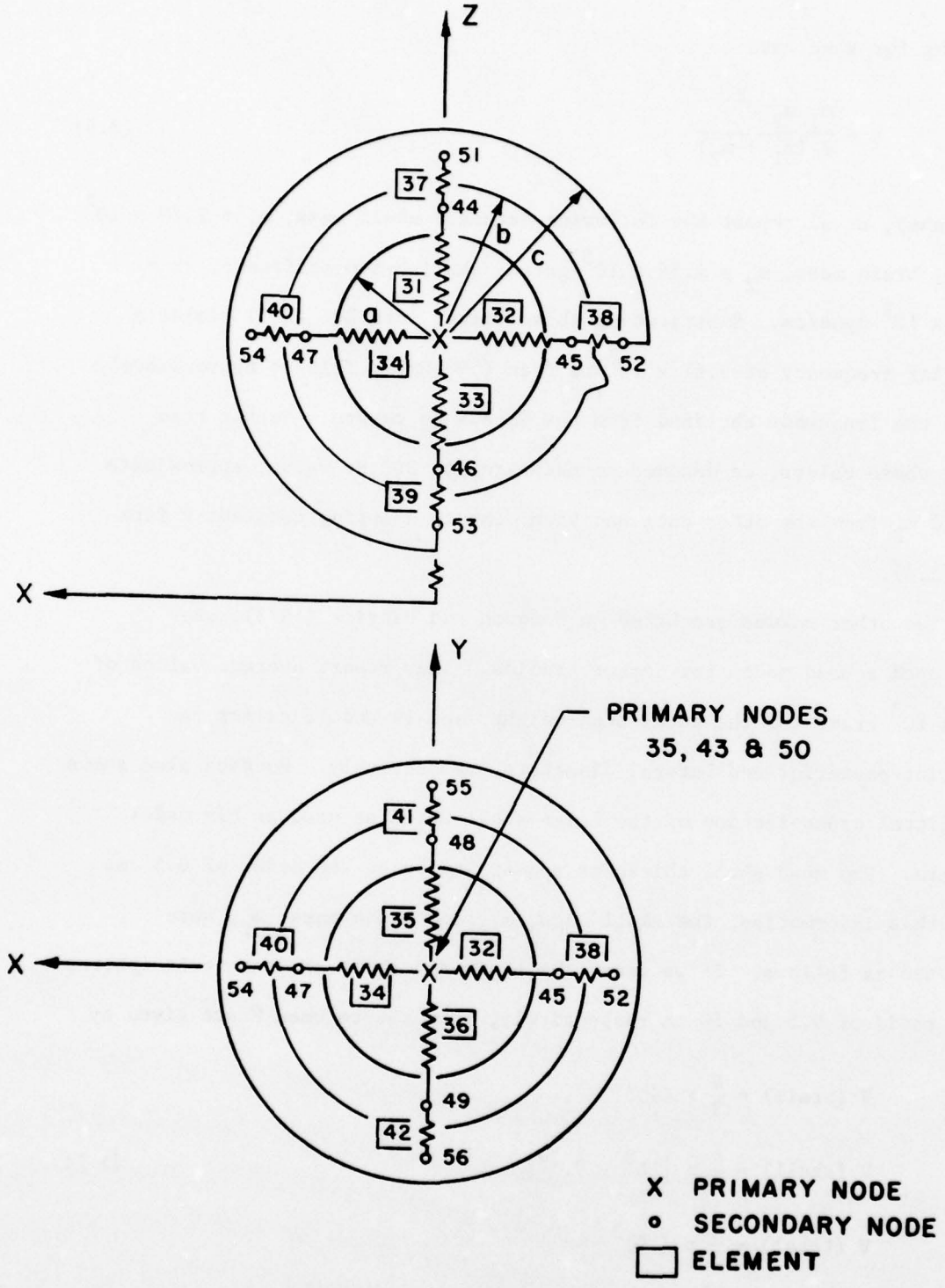

Figure 3.3 Head with helmet and brain for MSC injury model.

Solving for k we have

$$k = \frac{m_1 \, m_2 \, \Omega^2}{2 \, (m_1 + m_2)} \tag{3.6}$$

McElhaney, et al report the following values: skull mass, $m_1 = 2.72 \times 10^2$ grams, brain mass, $m_2 = 4.54 \times 10^3$ grams, skull-brain stiffness, $2k = 3.45 \times 10^9$ dyne/cm. Substituting these values into Eq. (3.5) yields a circular frequency of 3.67×10^3 rad/sec (580 Hz). This is approximately twice the frequency obtained from the impedance curves. Rather than using these values, we decided to maintain the 300 Hz value, approximate m_1 and m_2 from the other data and then compute a spring constant k from Eq. (3.6).

The other values are based on Hodgson and Patrick (1973), who developed a head model for impact studies. They report average values of 4.6×10^3 grams for the total head weight, and 19 and 16 cm for the anterior-posterior and lateral diameters, respectively. Hodgson also shows a sagittal cross-section of the human skull which he used as his model pattern. The mean skull thickness appears to be on the order of 0.5 cm. From this information, the skull mass, m_1, and brain mass, m_2, were computed as follows. If we treat the brain and skull as concentric spheres with radii of 9.5 and 10 cm respectively, then the volumes V are given by

$$\begin{aligned} V \text{ (brain)} &= \frac{4}{3} \pi \, (9.5)^3 \\ V \text{ (skull)} &= \frac{4}{3} \pi \, [10^3 - 9.5^3] \\ V \text{ (total)} &= \frac{4}{3} \pi \, (10)^3 \end{aligned} \tag{3.7}$$

Hence the ratios are

$$V \text{ (brain)}/V \text{ (total)} = 0.857$$

$$V \text{ (skull)}/V \text{ (total)} = 0.143$$

Assuming a constant density for the skull and the brain and a total head mass of 4.6×10^3 grams, m_1 and m_2 are given by

$$m_1 = (.143)\ (4.6 \times 10^3) = 6.57 \times 10^2 \text{ grams}$$

$$m_2 = (.857)\ (4.6 \times 10^3) = 3.94 \times 10^3 \text{ grams}$$

With these values for m_1 and m_2, Eq. (3.6) yields a value of 1.00×10^9 dyne/cm for the springs connecting the two masses.

The rotational inertias of the brain and skull were computed as follows. The rotational inertias of a solid sphere, I_S, and a hollow sphere, I_H, are given by

$$I_S = 2mr^2/5 \tag{3.8a}$$

$$I_H = 8m\pi\ (r_o^5 - r_i^5)\ /\ 15\ V \tag{3.8b}$$

Eqs. (3.8a) and (3.8b) yield values of 1.42×10^5 and 3.79×10^4 gram-cm^2 for the brain and skull respectively.

The values used for the translational and rotational masses of the helmet were those reported by Belytschko, et al (1976),

$$m = 1.40 \times 10^3 \text{ grams}$$

$$I = 1.00 \times 10^5 \text{ gram-cm}^2$$

The spring constants for the springs connecting the helmet to the head were determined as follows. The material of the interior of the helmet was taken to be styrofoam. A specific value for the Young's

Table 3.3: Stiffness and Intertial Properties of Brain/Skull/Helmet Head Impact Model

	Linear Stiffnesses dyne/cm	Translational mass (grams)	Rotational mass (gram-cm^2)
Brain	1.00×10^9	3.94×10^3	1.42×10^5
Skull	rigid	6.57×10^2	3.79×10^4
Helmet	$4.48 \times 10^{9(1)}$	1.40×10^3	1.00×10^5

(1) stiffness in compression only

modulus is not available because styrofoam is a porous styrene matrix and its mechanical properties are functions of density.

A cubic load-deflection relationship was used

$$f = (k + K\ 10^2\ \delta^2)\ \delta \tag{3.9}$$

The Young's moduli for synthetic rubbers have a range of approximately 500-10,000 psi. Based on this, the Young's modulus was taken to be 500 psi (1.75×10^7 dyne/cm^2). The linear stiffness of each of the 6 helmet spring elements is then given by

$$k = \frac{AE}{6L} = 4.48 \times 10^9 \text{ dyne/cm}$$

where A is total surface area of the middle surface of the helmet which is 1.52×10^3 cm^2. Table 3.3 summarizes the stiffness and inertial properties of the brain-skull-helmet (BSH) system.

From one dimensional modal analyses of the SSM with the brain-skull-helmet (BSH) head impact model, it was determined that the natural frequency of the brain-skull representation is approximately 300 Hz for motion in all three global coordinate directions. The stiffness proportional damping parameter for the brain elements was based on 50% damping of this frequency,

$$\alpha = \frac{1}{2\ \pi\ (300)} = 5.31 \times 10^{-4}$$

The damping ratio reported by McElhaney, et al was approximately 0.20, while the damping ratios used by some other investigators were 0.40, 0.707 and 1.0 (as reported by McElhaney, et al).

In order to study the behavior of this model, several simulations were performed on the head-spine model alone with initial velocities

prescribed to the helmet. For the first simulation, an initial velocity vector of

$$\vec{V}_o = (-0.707\ \vec{i} - 0.707\ \vec{k})\ (4.47 \times 10^3)\ \text{cm/sec}$$

($|\vec{V}_o|$ = 100 mph) was prescribed at the helmet; the head was 2 in. (5.08 cm) forward from the seatback; the SSM was fixed at the pelvis; a restraint system consisting of two seatbelts between the seatback and the pelvis was included; the solution time increment was 2.0×10^{-5} sec and 600 time steps were used for a duration of 0.012 sec.

Tables 3.4 and 3.5 list the peak values of some of the motion and force responses respectively. For comparison, Table 3.6 lists some of the peak motion and force responses from a similar simulation with the SSM with a single rigid body representing the head and helmet. Figure 3.4 depicts the SSM configurations at 0, 4, 8, and 12 milliseconds.

A comparison of the results given in Tables 3.4 and 3.5 demonstrate that considerably more energy is transmitted to the body through the rigid head/helmet than through the BSH. This is to be expected since some of the impact energy goes into deformation of the BSH elements.

The remaining five impact simulations consisted of varying the initial helmet velocities through magnitudes of 2235, 1118, 559, 279 and 140 cm/sec (50, 25, 12.5, 6.25 and 3.125 mph respectively). These initial helmet velocities correspond to 2.62×10^9, 1.24×10^9, 6.11×10^8, 3.06×10^8 and 1.53×10^8 dyne forces, respectively (5890, 2788, 1374, 688 and 344 lbs, respectively.) These were short duration (0.0002 sec.) simulations since the quantities of primary interest were the peak strains in the springs representing the skull-brain system, which occur early in the simulation. Table 3.6 summarizes the brain element strains for all

the simulations. The numbers given are the averages of the peak strains in the top, front, bottom and rear brain elements.

The strains vary almost linearly with initial helmet velocity or helmet impulse, particulary for lower levels. Linear interpolation between the lowest two values results in an initial helmet velocity of 210 cm/sec (4.70 mph) and a helmet force of 2.74×10^8 dyne (617 lbs) for a strain equal to the MSC value of 0.0061. These two values represent the cut-off levels between reversible and irreversible brain damage as predicted by the present BSH model. It should be noted that these values are most likely conservative since the elasticity of the brain was represented by linear springs. In reality, the stiffness of the brain tissue would increase with increasing deformation resulting in smaller strains that those predicted by a linear spring model.

Table 3.4: Peak Motion Responses for Brain-Skull-Helmet Impact Simulation,

$\vec{V}_o = (.707\ \hat{j} - .707\ \hat{k})\ 4.47 \times 10^3$ cm/sec

Peak Motion Response	
Helmet:	
y displacement	5.80 cm
z displacement	-1.37 cm
x rotation	0.66 rad
y acceleration	-8.68×10^6 cm/sec^2
z acceleration	9.57×10^6 cm/sec^2
x rotational acceleration	7.02×10^4 rad/sec^2
Skull:	
y displacement	5.80
z displacement	-4.04
x rotation	-0.35
y acceleration	1.47×10^7
z acceleration	-1.36×10^7
x rotational acceleration	-2.18×10^5
Brain:	
y displacement	5.87
z displacement	-4.09
x rotation	0.0
y acceleration	7.27×10^5
z acceleration	-6.31×10^5
x rotational acceleration	0.0

Table 3.4: Continued

Peak Force Response	
T1-C6:	
axial force	-1.23×10^{9} dyne
shear force	-2.60×10^{8} dyne
sagittal moment	7.80×10^{8} dyne-cm
C6-C4:	
axial force	-1.42×10^{9}
shear force	-3.82×10^{8}
sagittal moment	-1.20×10^{9}
C4-Skull:	
axial force	-2.62×10^{9}
shear force	1.65×10^{9}
sagittal moment	-4.18×10^{9}
Helmet-Skull element forces (dyne)	
top	-1.59×10^{10}
front	-1.48×10^{10}
bottom	-2.36×10^{9}
rear	-2.62×10^{9}
Skull-Brain element forces (dyne)	
top	-1.20×10^{9}
front	-1.40×10^{9}
bottom	1.28×10^{9}
rear	1.51×10^{9}

Table 3.4: Continued

Skull-Brain element strains ($^{cm}/_{cm}$)

top	-.0748
front	-.1058
bottom	.0861
rear	.1122

Table 3.5: Peak Force And Motion Responses For Rigid Head Impact Simulation,

$\vec{V}_o = (.707\ \hat{j} - .707\ \hat{k})\ 4.47 \times 10^3$ cm/sec

Head/Helmet:	
y displacement	6.84 cm
z displacement	-16.60 cm
x rotation	-.42 rad
y acceleration	-4.16×10^6 cm/sec^2
z acceleration	9.89×10^5 cm/sec^2
x rotational acceleration	-3.24×10^4 rad/sec^2
T1-C6:	
axial force	-2.08×10^9 dyne
shear force	-7.13×10^8 dyne
sagittal moment	2.80×10^9 dyne-cm
C6-C4:	
axial force	-2.27×10^9
shear force	-8.73×10^8
sagittal moment	2.08×10^9
C4-Head:	
axial force	-4.36×10^9
shear force	3.13×10^9
satittal moment	-8.20×10^9

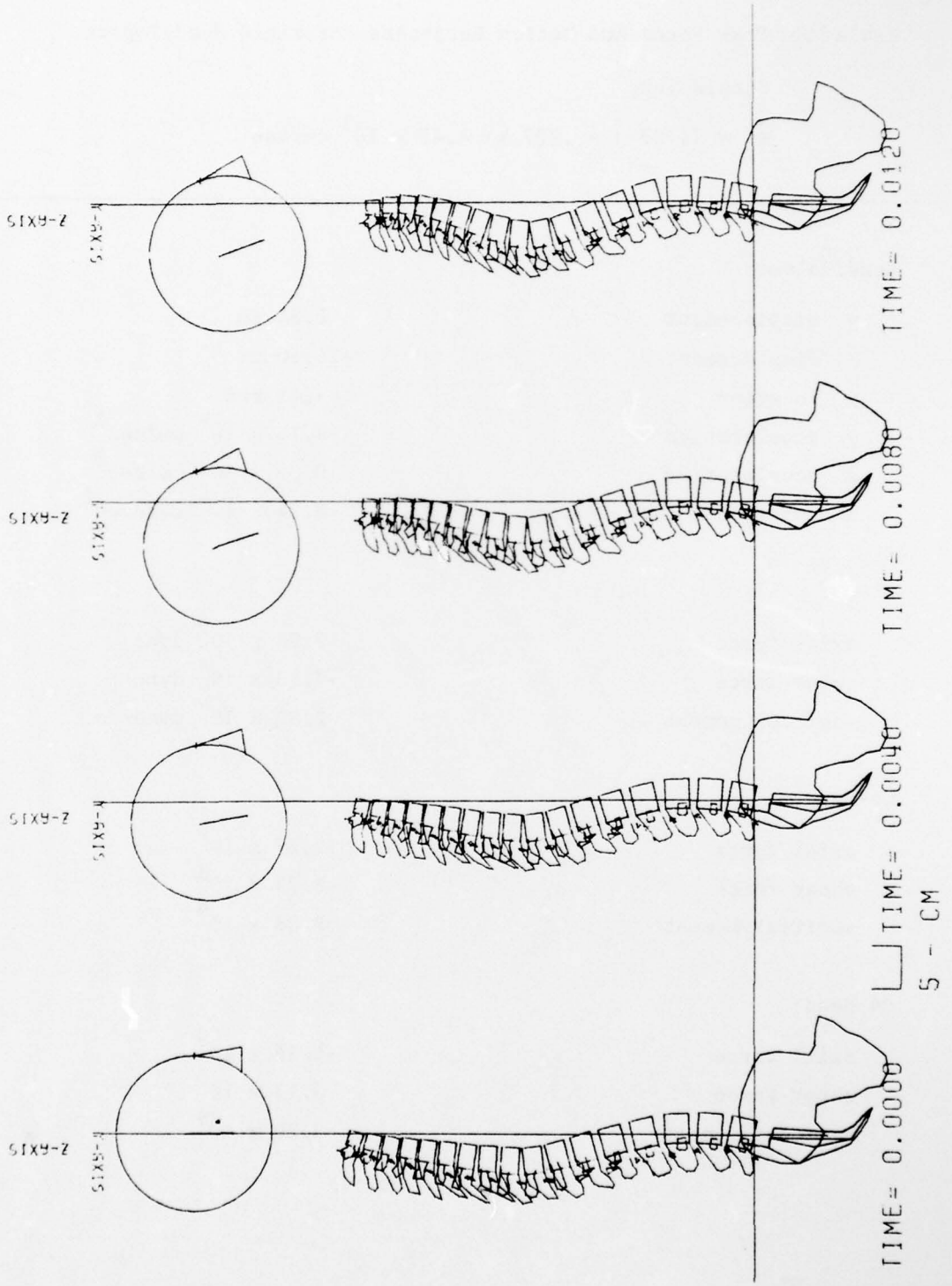

Figure 3.4 Initial, 0.004, 0.008, and 0.012 sec SSM configurations: initial helmet velocity = $(-0.707\,\vec{i} - 0.707\,\vec{k})$ 4.47×10^3 cm/sec (100 mps); helmet impulse = 6.44×10^9 dynes (1.45×10^4 lbs).

Table 3.6: Strains Occurring in Brain Elements

Initial Helmet Velocity		Helmet Impulse F_o		Average Peak Brain Element Strain
cm/sec	mph	dyne-sec	lbs-sec	
4470	100	6.44×10^9	1.45×10^4	0.0947
2235	50	2.62×10^9	5890	0.0506
1118	25	1.24×10^9	2788	0.0264
559	12.5	6.11×10^8	1374	0.0135
279	6.25	3.06×10^8	688	0.0068
140	3.125	1.53×10^8	344	0.0034

SECTION 4

CANOPY MODEL

4.1 Elastic Plastic Material Law

The initial specifications provided by WPAFB defined the material as a Ramberg-Osgood elastic-plastic material. Since an elastic-plastic material with a piecewise linear hardening curve was already available in SADCAT, the Ramberg-Osgood curve was approximated by straight line segments, so making possible the use of the available stress-strain law.

In this stress strain law, plastic yielding is defined by a Mises yield condition F, which in plane stress is

$$F\left(\{\sigma\}\right) = \sigma_x^2 - \sigma_x\sigma_y + \sigma_y^2 + 3\sigma_{xy}^2 \leq \bar{\sigma}^2 \tag{4.1}$$

where $\bar{\sigma}$ is the yield stress, which is initially σ_Y but increases as the material strain hardens. In a corotational formulation, the corotational stresses $\hat{\sigma}$ are used, but the hats are here omitted for convenience. In an elastic-plastic law, the strain increments are additively decomposed into elastic strain increments $\Delta\epsilon^e$ and plastic strain increments $\Delta\epsilon^p$, and the stress increments are related to the elastic strain increments so that

$$\{\Delta\sigma\} = [C]\left(\{\Delta\epsilon\} - \{\Delta\epsilon^p\}\right) \tag{4.2}$$

where

$$[C] = \frac{E}{1-\nu^2}\begin{bmatrix} 1 & \nu & 0 \\ \nu & 1 & 0 \\ 0 & 0 & (1-\nu)/2 \end{bmatrix} \tag{4.3}$$

where E is Young's modulus and ν is Poisson's ratio. The plastic strains are given by

$$\left\{\dot{\epsilon}^p\right\} = \dot{\lambda}\ H\ (\sigma_y)\ \left\{G\right\} \tag{4.4}$$

$$\dot{\lambda} = \begin{cases} 0 \text{ if } F \leq \sigma_Y^{\,2} \text{ or } \dot{F} < 0 & \text{(elastic)} \\ 1 \text{ if } F = \sigma_Y^{\,2} \text{ and } \dot{F} \geq 0 & \text{(plastic)} \end{cases}$$

$$\left\{G\right\} = \begin{Bmatrix} \partial F/\partial\sigma_x \\ \partial F/\partial\sigma_y \\ \partial F/\partial\sigma_{xy} \end{Bmatrix} = \begin{Bmatrix} 2\sigma_x - \sigma_y \\ 2\sigma_y - \sigma_x \\ 6\sigma_{xy} \end{Bmatrix} \tag{4.5}$$

and H is the hardening function; by prescribing H to be a function of only the yield stress, we restrict ourselves to isotropic hardening.

The incremental relation between stress and strain is then given by

$$\left\{\Delta\sigma\right\} = [C^p]\ \left\{\Delta\epsilon\right\} \quad \text{if plastic} \tag{4.6}$$

$$\left\{\Delta\sigma\right\} = [C]\ \left\{\Delta\epsilon\right\} \quad \text{if elastic}$$

where

$$[C^p] = [C] - \frac{[C]\ \left\{G\right\}^T\left\{G\right\}\ [C]}{H} \tag{4.7}$$

$$H = \left\{G\right\}^T[C]\ \left\{G\right\} + \left(\frac{2\bar{\sigma}}{3}\right)^3 E_p \tag{4.8}$$

where E_p is the current plastic modulus for the uniaxial stress-strain curve.

4.2 Nonlinear Elastic Law

An elastic-plastic material, when subjected to large displacements, maintains permanent large deformations because the elastic recovery is very small. An examination of the canopy response observed in experiments revealed that the canopy exhibited little permanent deformation even when the maximum displacements were very large. Therefore, a nonlinear elastic law was incorporated in the program for the

later computations.

In this law, the elastic law

$$\{\sigma^e\} = [C]\{\varepsilon\} \tag{4.9}$$

is used when the deviatoric stress invariant, Eq. (4.1), is less than the yield stress σ_Y. When σ_Y is exceeded, the additional stress is related to any additional strain through a matrix $[C^*]$ given by

$$[C^*] = \frac{E_p}{E}[C] \tag{4.10}$$

where E_p is the softer modulus. For these purposes, a portion of the stresses governed by Eq. (4.9), α must be computed by

$$\alpha = \frac{\sigma_Y}{\bar{\sigma}} \tag{4.11}$$

The total stress is then given by

$$\{\sigma\} = [C]\left(\{\varepsilon\} - \{\varepsilon_o\}\right) + \{\sigma_o\} \tag{4.12}$$

where

$$\{\sigma_o\} = \alpha\{\sigma\} \tag{4.13}$$

and

$$\{\varepsilon_o\} = [C]^{-1}\{\sigma_o\} \tag{4.14}$$

where

$$[C]^{-1} = \frac{1}{E}\begin{bmatrix} 1 & -\upsilon & 0 \\ -\upsilon & 1 & 0 \\ 0 & 0 & 2(1+\upsilon) \end{bmatrix} \tag{4.15}$$

so, whenever σ_Y is exceeded

$$\{\sigma\} = \left[\frac{E_p}{E}(1-\alpha) + \alpha\right]\{\sigma^e\} \tag{4.16}$$

The computational procedure for evaluating the stresses is then:

1. given a state of strain, the trial stress $\{\sigma\}$ is computed by Eq. (4.9).

2. the deviatoric stress invariant associated with these trial stresses are computed by Eq. (4.1).
3. if the trial stresses do not exceed σ_Y, they are the correct stresses; otherwise the factor α is computed by Eq. (4.11).
4. the stresses and strains associated with the initial modulus are computed by Eqs. (4.13) and (4.14).
5. the total stresses are computed by Eq. (4.12).

4.3 Material Constants for Canopy

The uniaxial stress strain law provided by AMRL is shown in Fig. 4.1. Since the software used in this investigation assumed a piecewise linear approximation to the stress strain law, it was fit using the following constants:

$$E = 2.413 \times 10^{10} \text{ dynes/cm}^2$$

$$\upsilon = 0.31$$

$$E_p = 3.32 \times 10^{8} \text{ dynes/cm}^2$$

$$\sigma_Y = 6.76 \times 10^{8} \text{ dynes/cm}^2$$

A plot of the piecewise linear approximation to the uniaxial stress-strain curve is shown in Fig. 4.1 also.

The use of this approximation can be justified by the fact that in simulations where the canopy contacts the head, strains are on the order of 1% to 5%. For strains of this magnitude, the small discrepancies between the piecewise linear approximation and the Ramberg-Osgood fit should be of little importance.

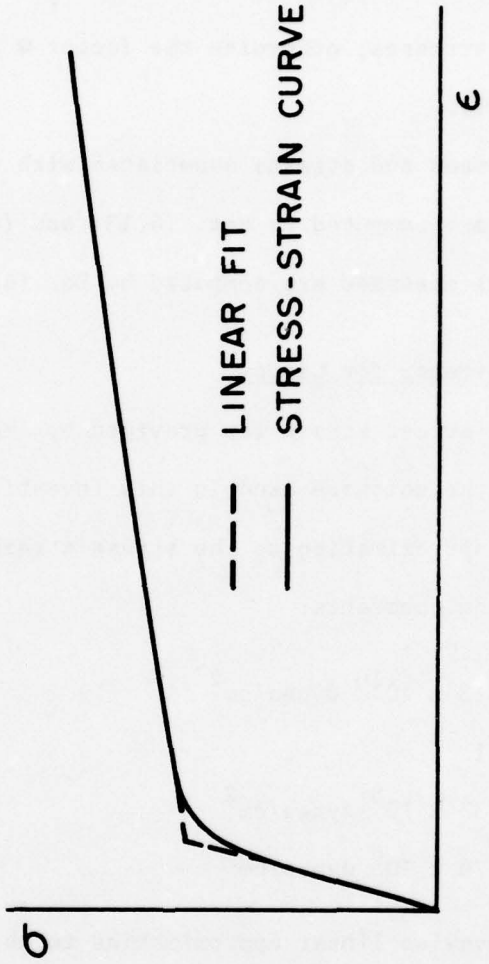

Figure 4.1 Piecewise Linear Fit To Stress-Strain Curve

SECTION V

RESULTS OF SIMULATIONS

5.1 Bird-Canopy Simulations

For the purpose of determining the mesh refinement needed in the canopy and the validity of the bird-impact model, we made a series of preliminary analyses with only the canopy, and no pilot. In these simulations, the bird was represented by a single pentahedral element with the following material constants

Bulk modulus = 2.6×10^{10} dynes/cm^2

Density = 1 gm/cm^3

Shear modulus = 0.0

A shear modulus could not be included because the pentahedral element does not account for shear stresses. The pentahedral element for the bird was then sized so that the desired mass was represented.

In these simulations, the canopy material was an uncoated monolithic polycarbonate, 1.27 cm (½ in) in thickness. Strain rate effects were not considered since they were incorporated in the material law provided, which is shown in Fig. 4.1. The elastic-plastic law was used. The initial fine canopy model is shown in Fig. 5.1, and the deformation is shown in Figs. 5.2 and 5.3 for the coarse and fine models. In this case, the bird mass was 0.98 kg (2.16 lbs) and its velocity was 177.7 m/sec in the horizontal direction. The point of impact was on the centerline of the canopy; location in the x-z plane is shown in the initial views of each of the canopies. Since the resulting problem was symmetric, only half of the canopy was modelled.

The maximum deflection for the 3 meshes are given in Table 5.1 and compared to the experimental result of Run GD1.

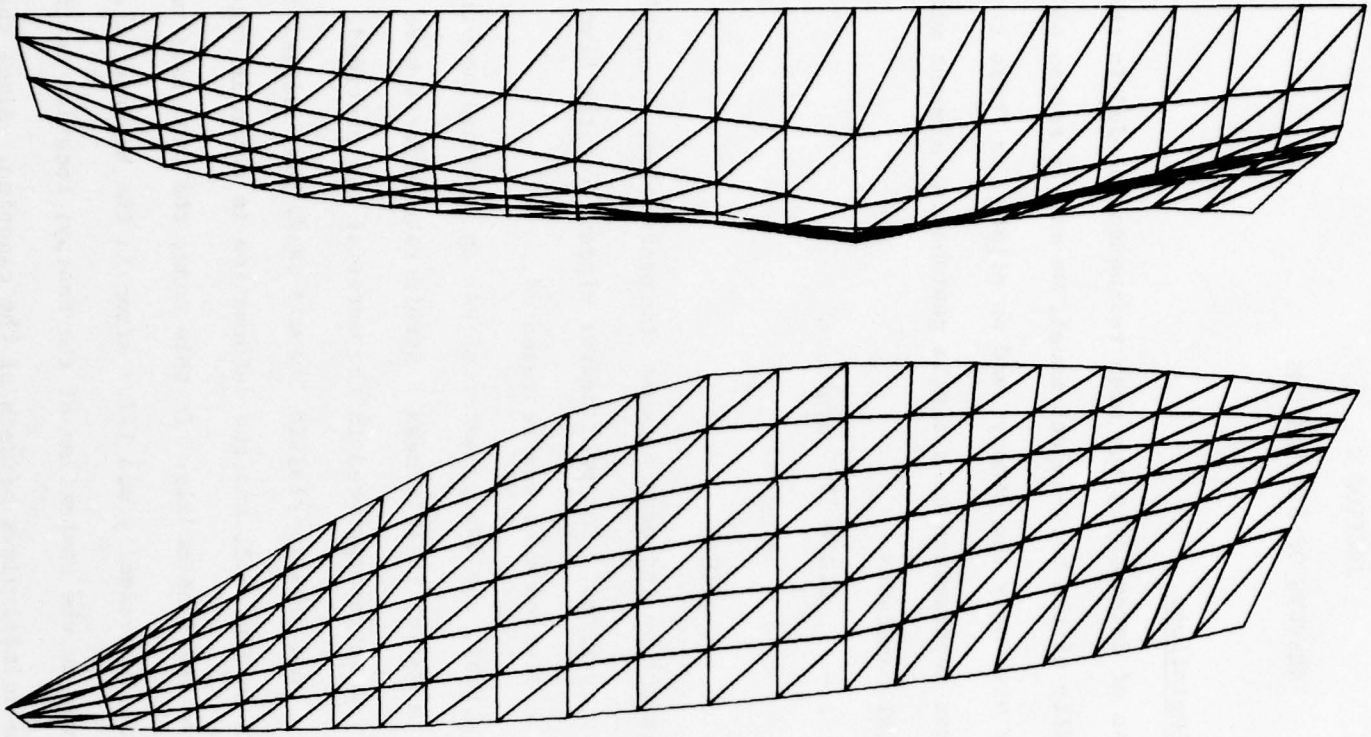

Figure 5.1 Top and Side View of Undeformed Fine Mesh Model

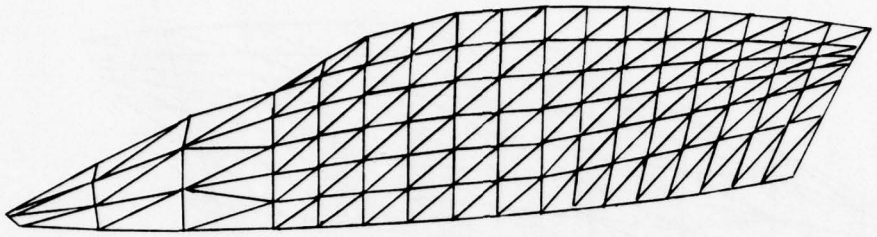

1.5 ms

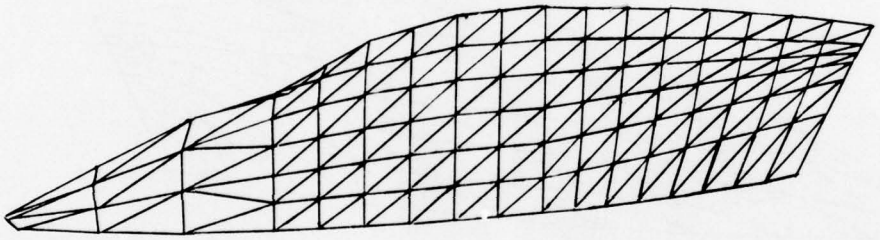

2.5 ms

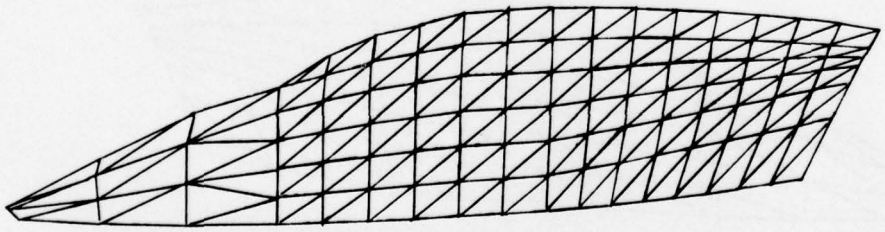

3.5 ms

Figure 5.2 Deformed Configurations of Fine Mesh Model

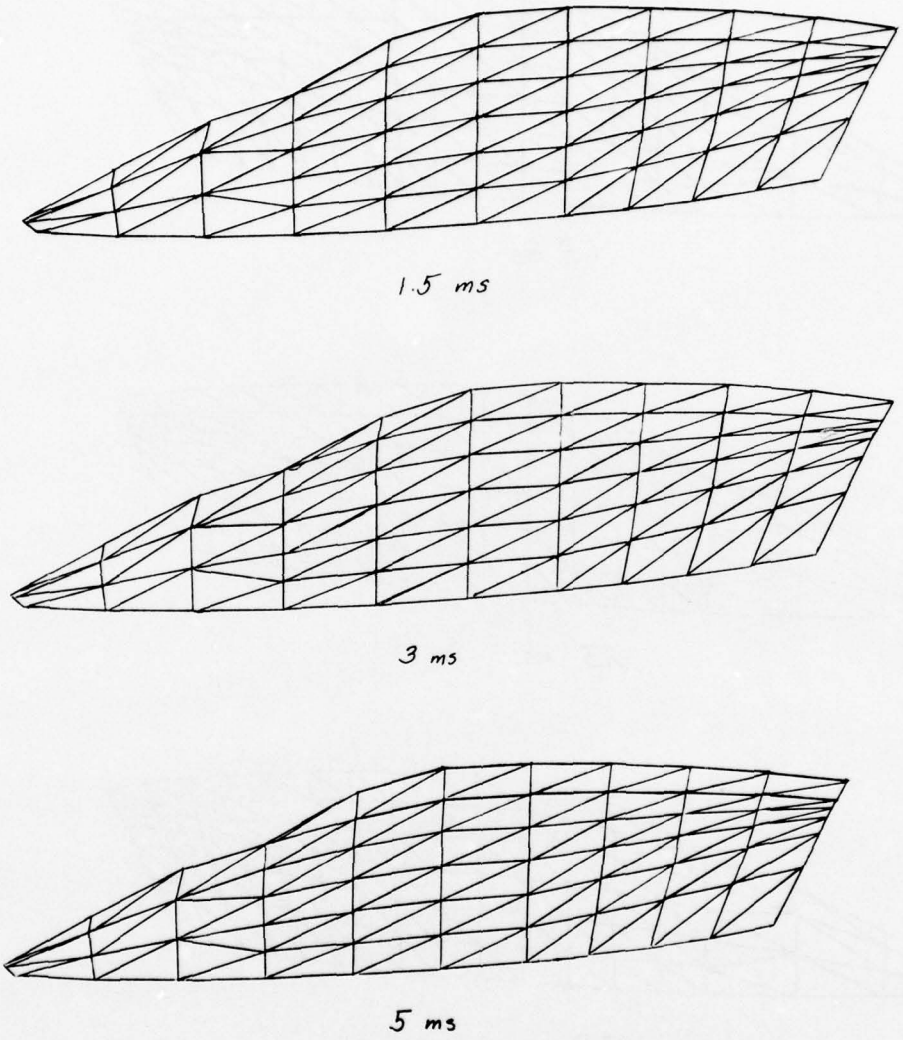

Figure 5.3 Deformed Configurations of Coarse Mesh Model

Table 5.1

Comparison of Maximum Deflections

	Coarse Mesh	Mixed Mesh	Fine Mesh	Experiment GD1
Maximum deflection	6.6 cm (2.8 in)	7.1 cm (2.8 in)	7.4 cm (2.9 in)	12.7 cm (5.0 in)

The maximum deflections underestimate the experimental value significantly, although the disparity decreases with mesh refinement. Unfortunately, the coarser meshes do not exhibit the wave pattern traveling along the canopy and even the fine mesh only exhibits the beginning of a wave which dies rapidly as it progresses. It could not be established whether this disagreement between the simulation and experiment was a result of an inadequate contact-impact model (i.e. neglecting friction and shear in the bird) or whether the canopy models were not sufficiently refined. The latter possibility could not be explored because the refined mesh used all available core; even it could not fit with the pilot model simultaneously.

Part of the problem was found to be due to the coarseness of the bird model. To illustrate this, we impacted a single mass point of the same mass as the bird (981 gm); at 26,822 cm/sec (521 Knots) against the canopy and compared an identical bird simulation with a pentahedron. The single point mass model of the bird yielded a maximum deflection of 20 cm, whereas the pentahedral model yielded a deflection of 12.9 cm. Evidently, the momentum of the back nodes of the pentahedron are not transferred to the canopy adequately. Furthermore, both models ricochet off the canopy after causing maximum deformation, thus eliminating the wave effect. The deflection

pattern for the single node bird model is shown in Fig. 5.4. The discrepancy between experiment and simulation lies in the failure of the plate elements along the subsequent path of the bird to deform prior to its arrival, thus causing a large slope in the subsequent path which causes the bird to ricochet. We were unable to determine whether this unfortunate phenomenon was due to insufficient discretization of the bird, canopy or both. However, in order to avoid this difficulty, we simulated the bird impact by prescribing an initial impulse to the impacted part of the canopy in most of the simulations and retained the contact-impact algorithm only for modelling canopy-helmet impact.

5.2 Canopy Impulse-Pilot Simulations

Only one simulation was successfully completed with a complete bird, canopy and pilot impact, but because at the time of its completion, computer generated graphic displays of the complete system were not available, so we will report it later in the section.

The first simulation obtained with a complete graphical display was a 114 kg-m/sec impulse applied normal to the canopy coarse mesh model, 32 cm anterior to the front of the pilot's helmet. The impulse given here is normal to the canopy and corresponds to a perfectly plastic, frictionless impact with a bird in a horizontal path with a momentum of 251 kg-m/sec; the difference between the momentum and the impulse reflects the angle of 27^{o} between the surface of the canopy and the horizontal axis. For a 0.98 kg bird (2.16 lbs), this corresponds to an initial velocity of 257 m/sec (500 knots), and a kinetic energy of 31.8×10^{3} N-m. For a 1.82 kg bird, this corresponds to an initial velocity of 138 m/sec (270 knots) and a kinetic energy of 17.3×10^{3} N-m.

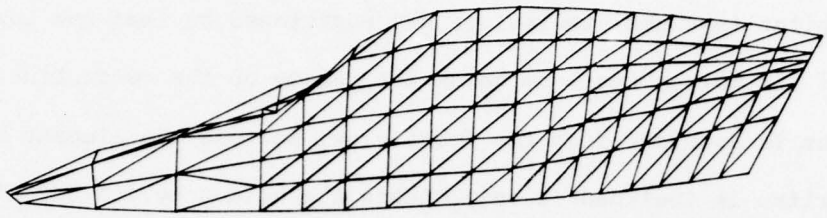

TIME 1E-03

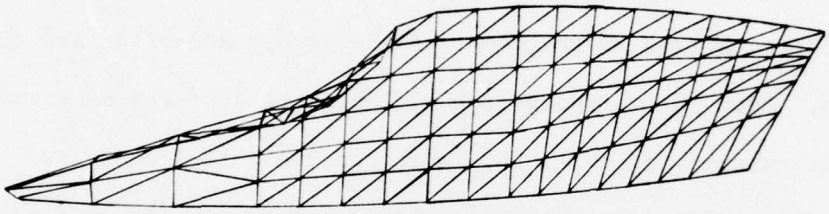

TIME 1.75E-03

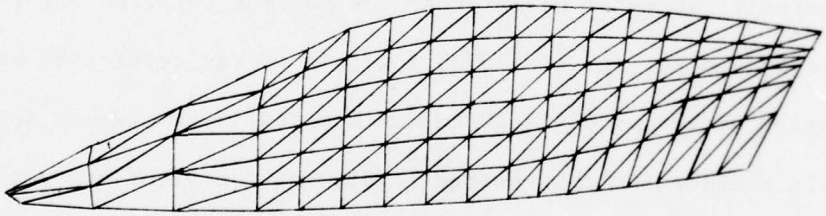

TIME 2E-04

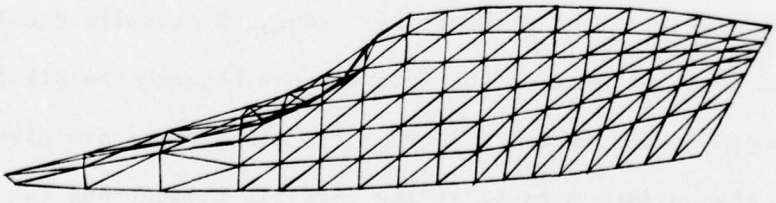

TIME 2.5E-03

Figure 5.4 High Velocity Bird Impact Simulation with Single Node Point Model of Bird

The latter corresponds closely to the USAF "goal" tolerance bird strike of a 1.8 kg bird at 350 knots.

The pilot in these simulations was positioned so that the top surface of his helmet was 5 cm below the canopy on the centerline; however, as is apparent from the front view, because the element by the centerline is inclined it only clears the helmet by 1.5 cm. The pilot's head was 5 cm anterior to the seat-back, so that initial lateral motions were not restrained by the seat-back.

The configurations of the model of the canopy and pilot are shown in Fig. 5.5. Note that although the elements are depicted as planar, with discontinuities in the slope, in the analysis the canopy is treated by cubic displacements which are almost completely continuously differentiable. The maximum deflection for this simulation is 22 cm, which is actually somewhat higher than the maximum reported for the experiments by Specker, et al (1978) for this energy level; Specker, et al reported approximately a 20 cm maximum and 15 cm maximum deflection at the pilot station for this energy level. At the pilot however, the maximum deflection obtained here is quite small ($\sim$ 8 cm) and the nodes behind the pilot hardly deflect at all; this is a consequence of the impulse simulation of bird strike. Thus, the results should be interpreted more in terms of the interference between the pilot's helmet and canopy (which is about 7 cm). The MSC results are given in Table 5.2; the maximum strains in the vertical element and the maximum strains in the anterior-posterior element are given. Lateral element strains were always almost zero because of symmetry. The MSC value represents the maximum of the square root of the sum of the strains.

Table 5.2

Maximum Strains Criterion for Simulations

Simulation Number	Canopy Impulse kg m/sec	Notes	Maximum Vertical Strains	Maximum Ant.-Post. Strains	Maximum Strain (MSC)
1	114		-5.9%	3.0%	6.4%
2	144	reduced canopy strength	-6.0%	3.2%	6.7%
3	85.5		-1.3%	0.5%	1.4%
4	85.5	pilot raised 1.0 cm	-3.7%	1.0%	4.0%

This simulation showed significant rotations of the pilot's head. This can be observed from the earline, which is coincident with the vertical axis in the undeformed display and at 0.25 m/sec. However, in the 0.63 and 1.0 m/sec displays the earline is displaced to the back and rotated counterclockwise. Since rotational accelerations are of importance in brain stem injuries and impairment but are not reflected in the MSC, the application of this injury criterion in future work on bird-strike should be re-examined.

The elastic-plastic law was used in this simulation, so as can be seen from Fig. 5.5 the canopy does not rebound to its initial shape.

It can be seen from Table 5.2 that the larger strains are in the vertical direction, reflecting the predominantly vertical direction of the impact to the helmet. The MSC is above the MSC criterion for irreversible injury of 6.1%.

Simulation 2 repeated the same impulse but the canopy yield stress and moduli that are given in Chapter 4 were reduced by 15%. The purpose of this simulation was to investigate the sensitivity of the results to the material properties of the canopy. As can be seen from Table 5.2 the change in the results is even smaller than the change in the material properties.

In simulation 3, an impulse of 85.5 m/sec was applied normal to the canopy at the same point as the previous simulations. The position of the pilot and the canopy properties were identical to simulation 2. However, a mixed mesh with smaller elements was placed in the vicinity of the pilot, and the nonlinear elastic law was used. This simulation reflects a bird with a horizontal momentum of 188 kg-m/sec,

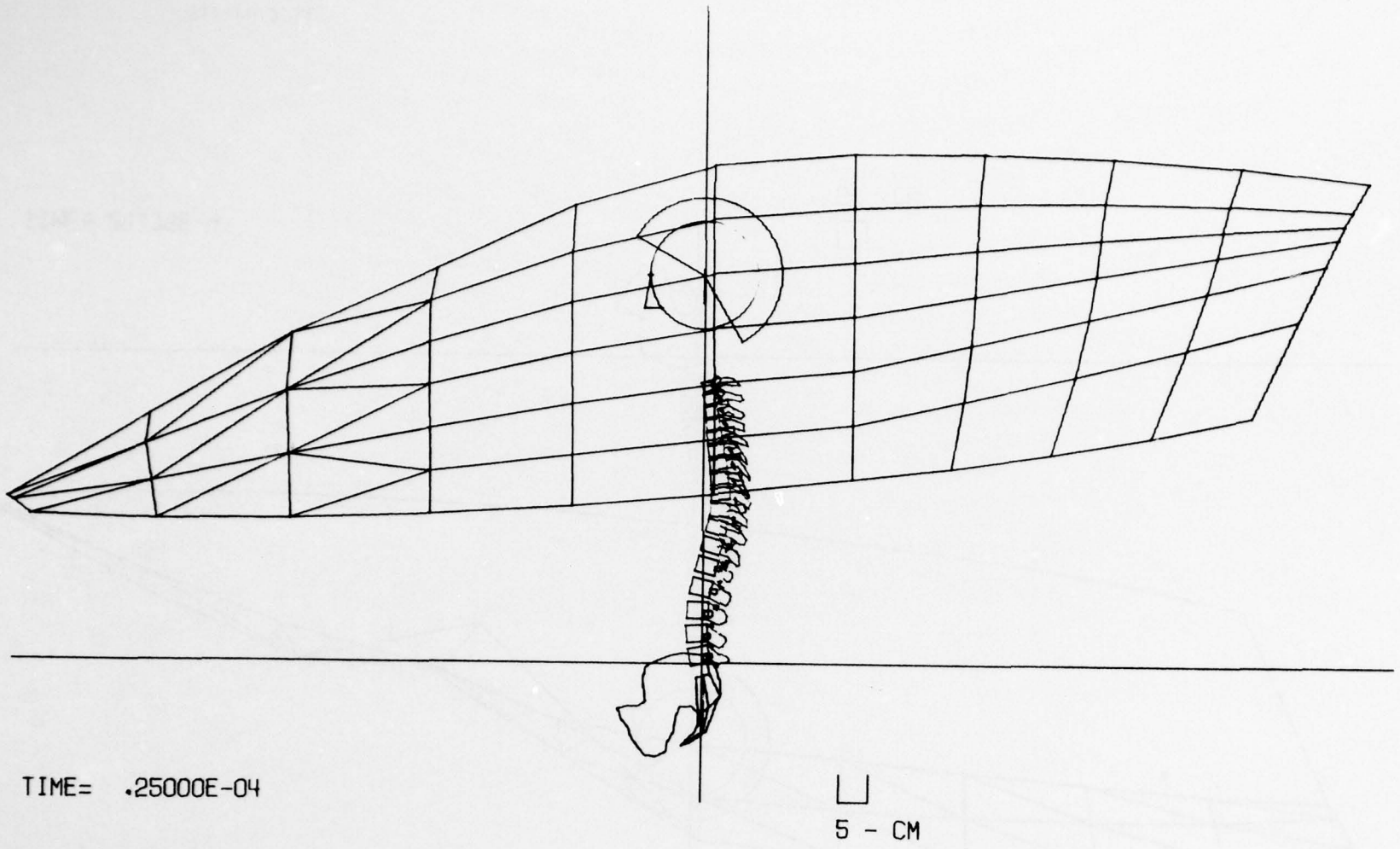

Figure 5.5 Response of Canopy and Pilot for 114 kg-s/sec Impulse (Simulation 1)

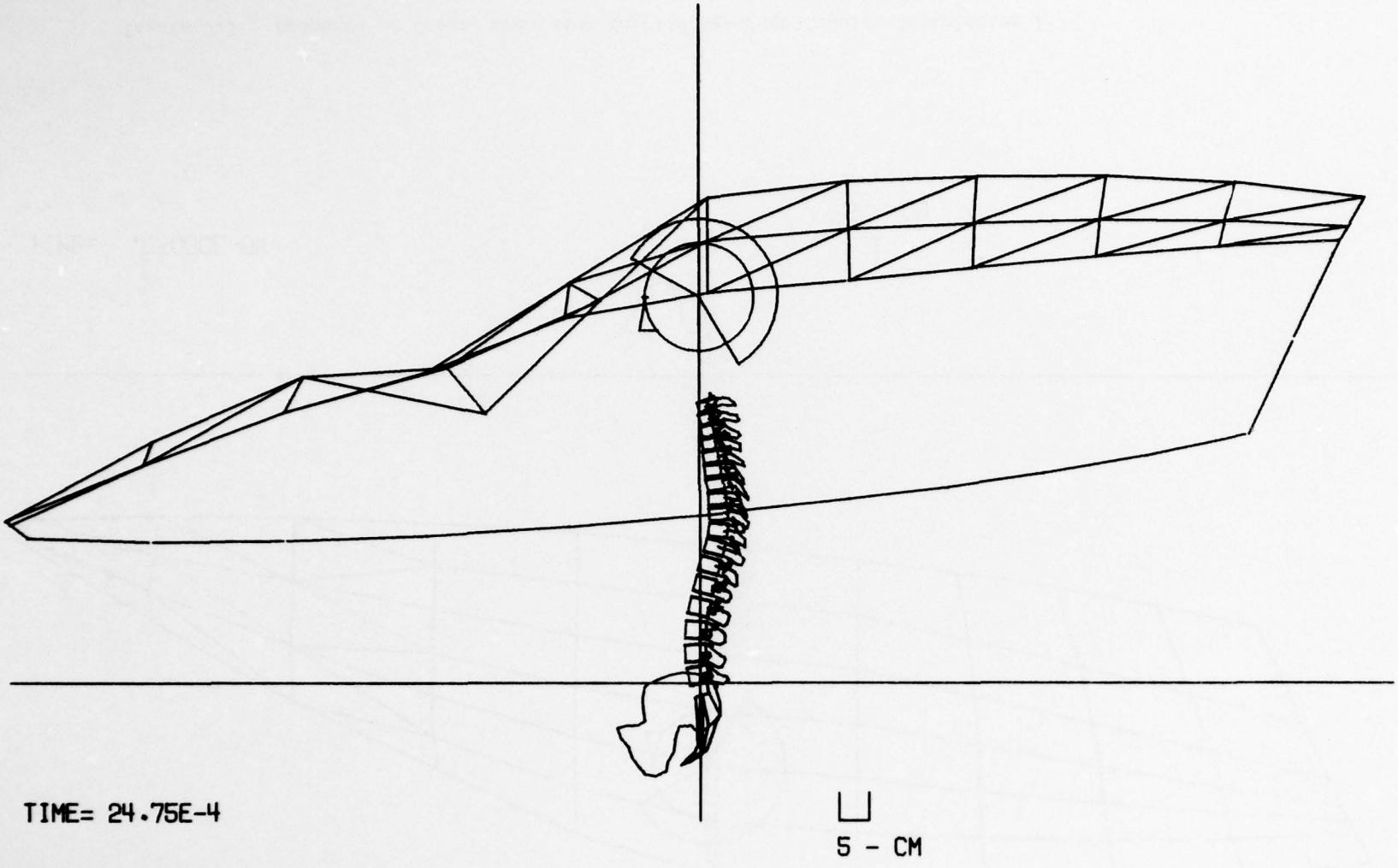

Figure 5.5a

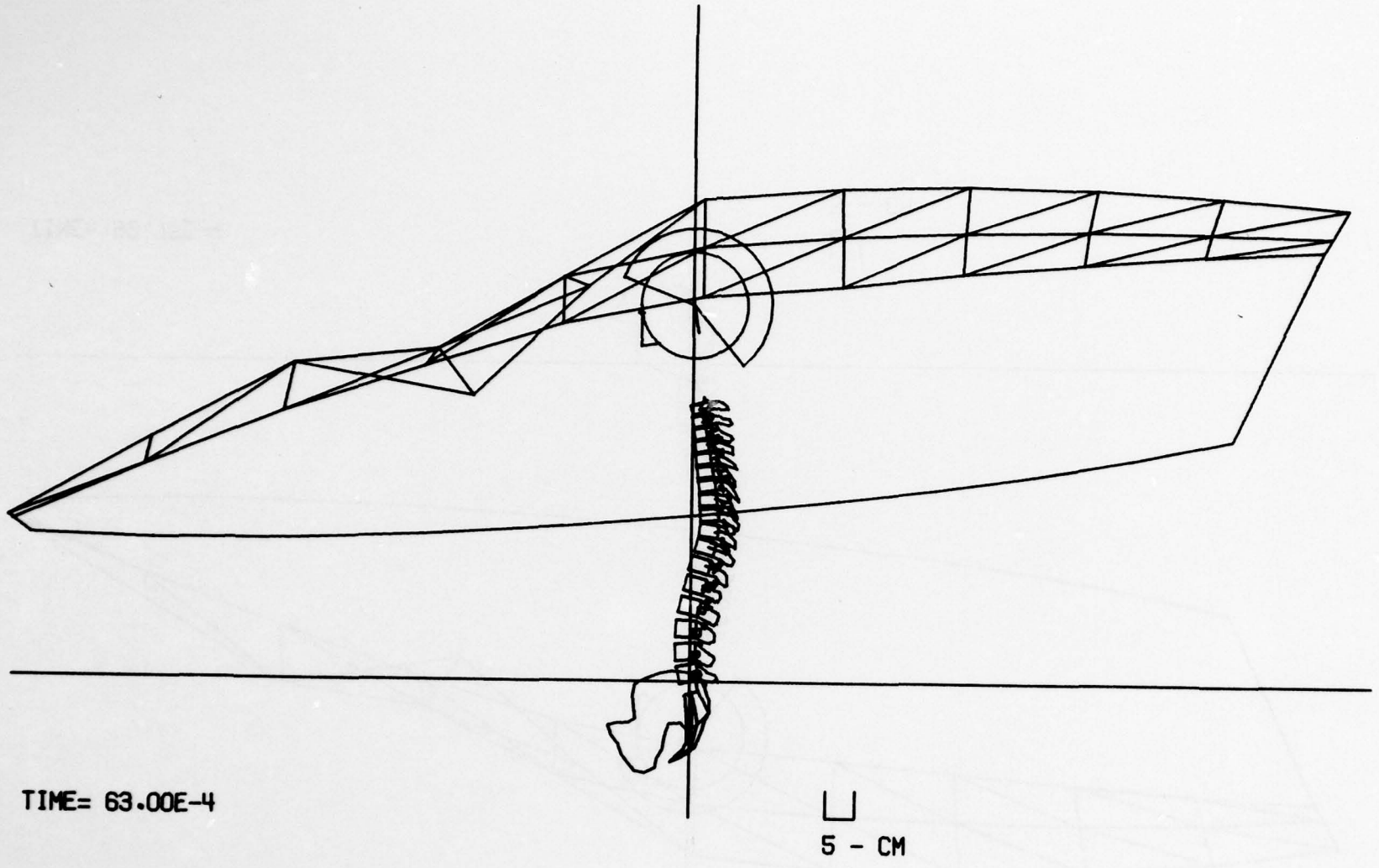

Figure 5.5b

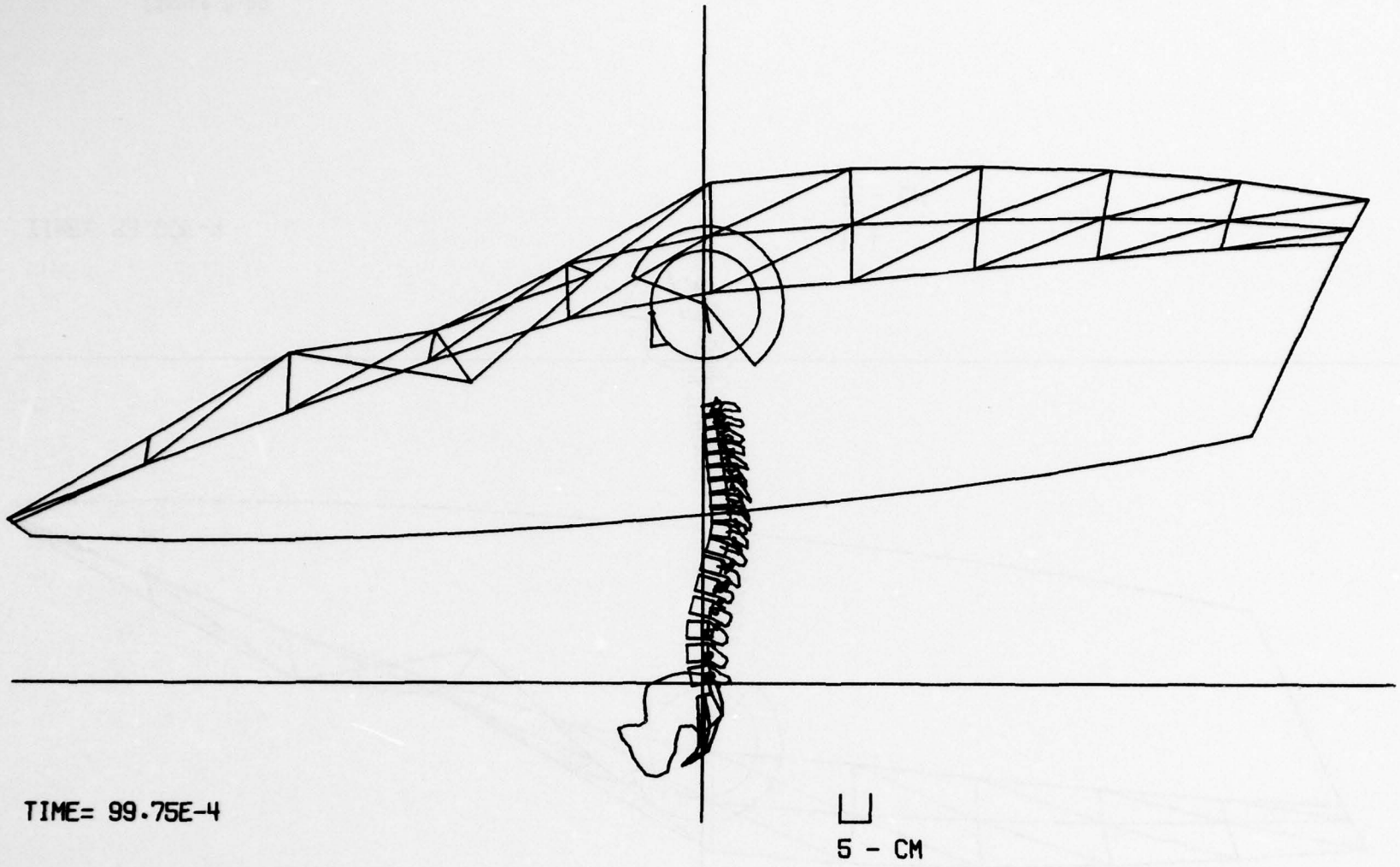

Figure 5.5c

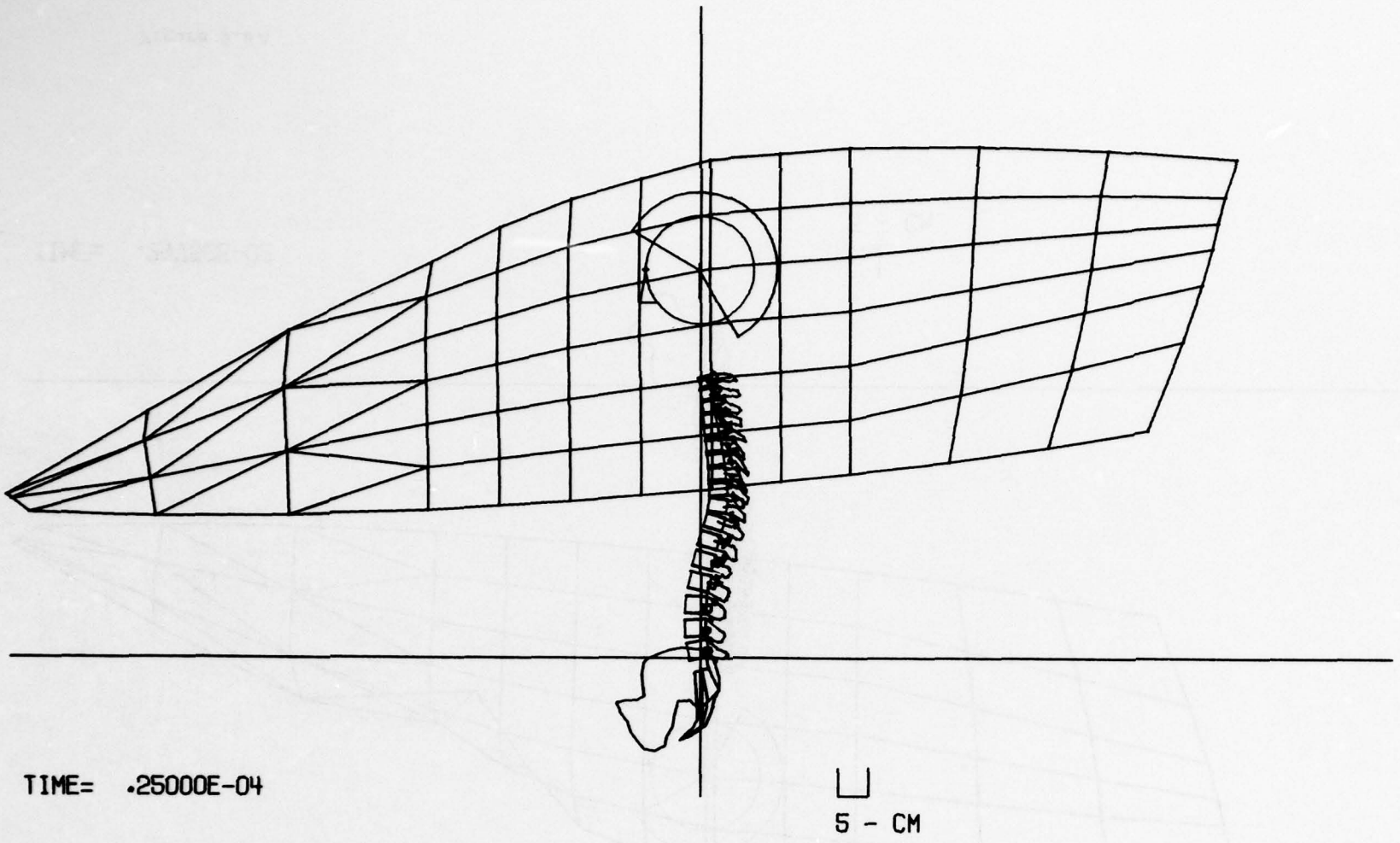

Figure 5.6 Response of Canopy and Pilot for 85.5 kg-m/sec Impulse (Simulation 3)

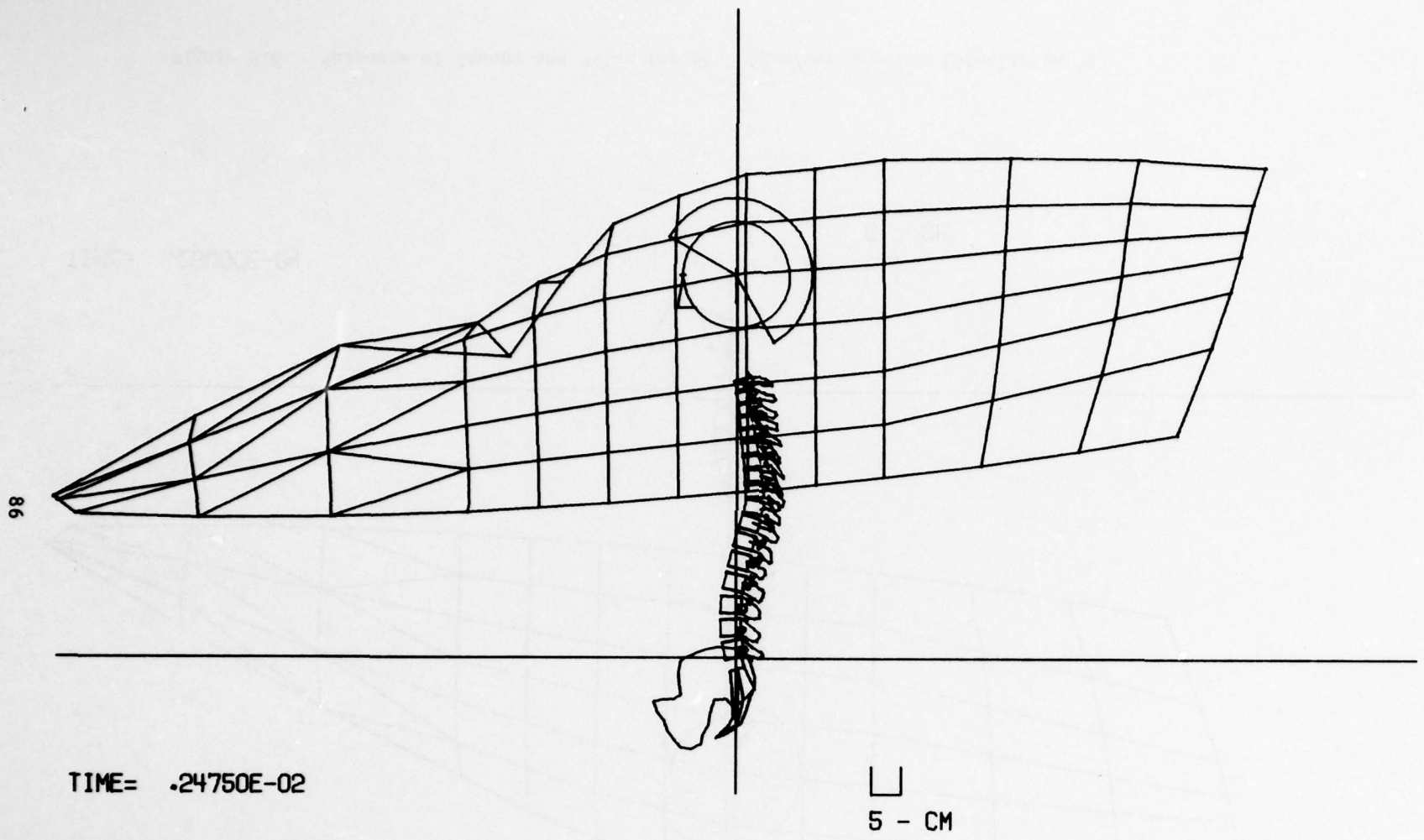

Figure 5.6a

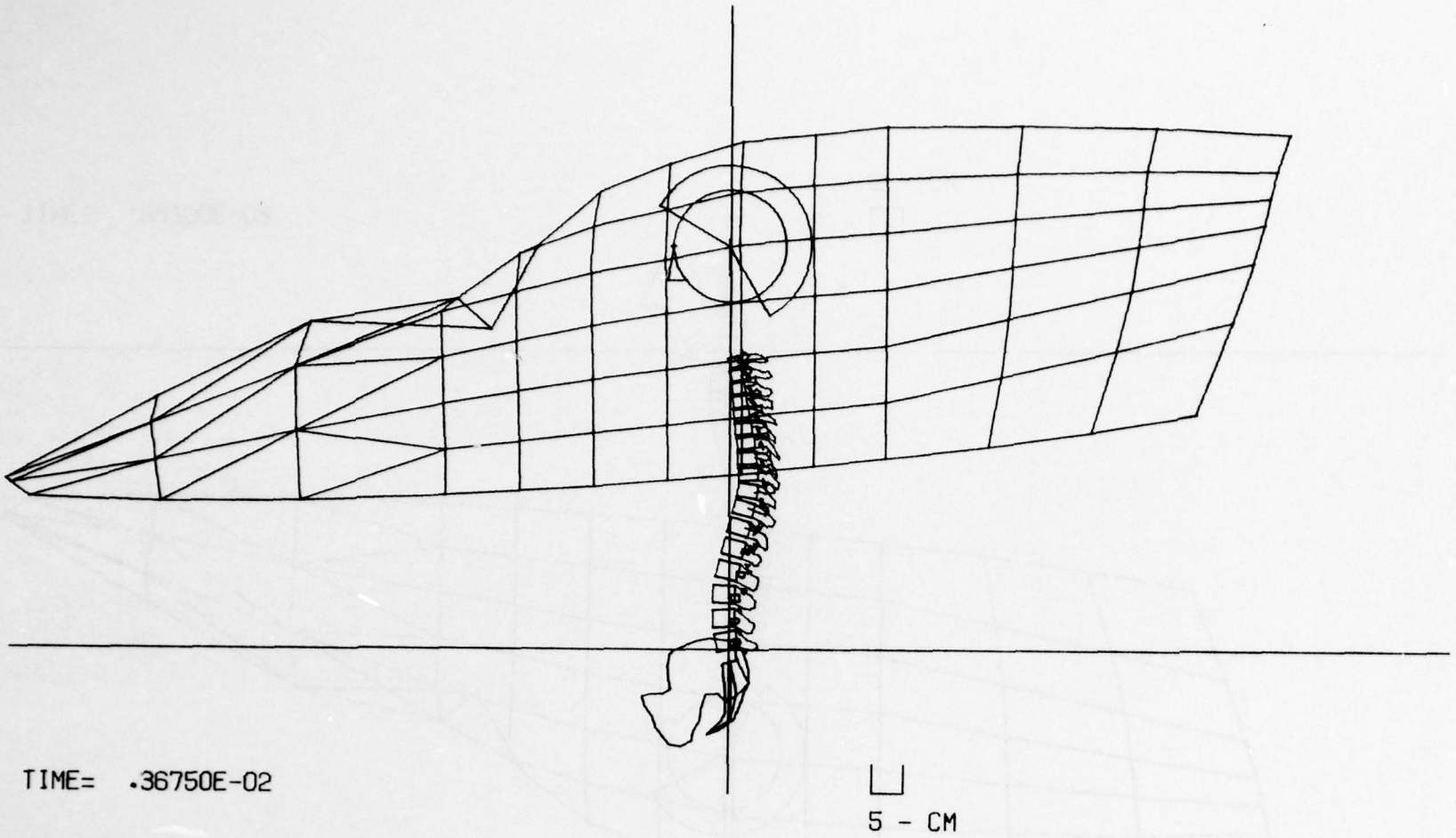

Figure 5.6b

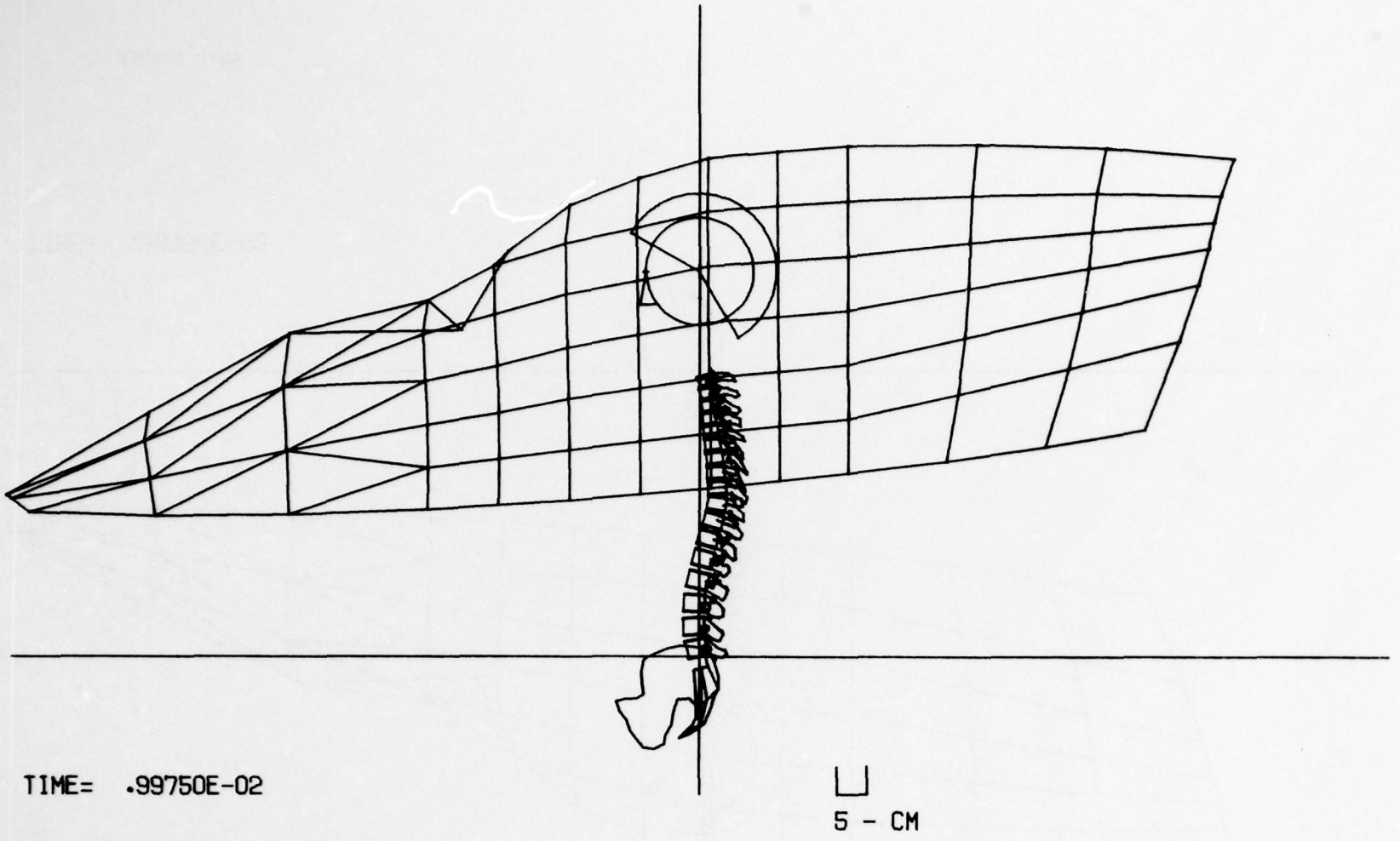

Figure 5.6c

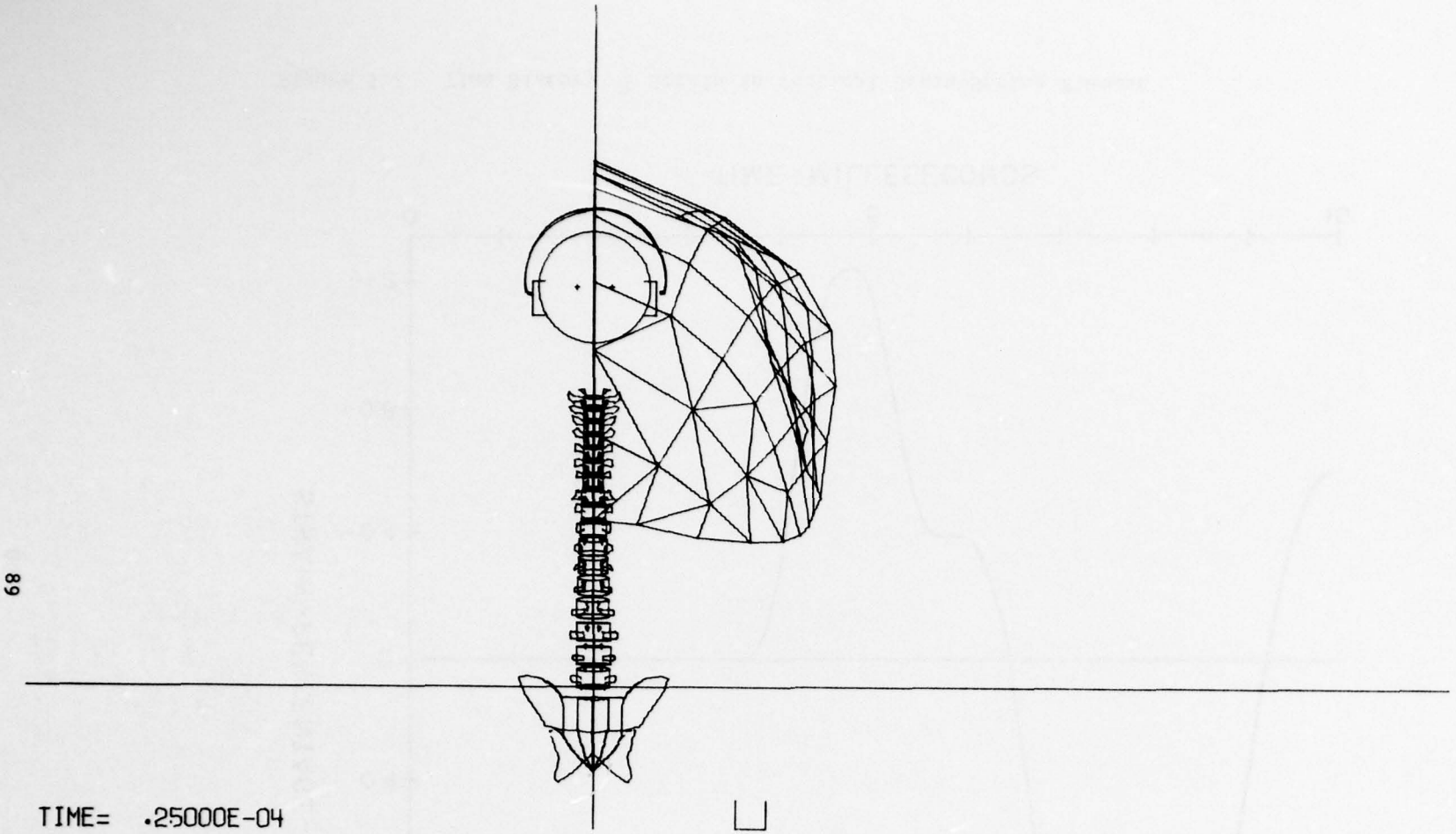

Figure 5.6 d

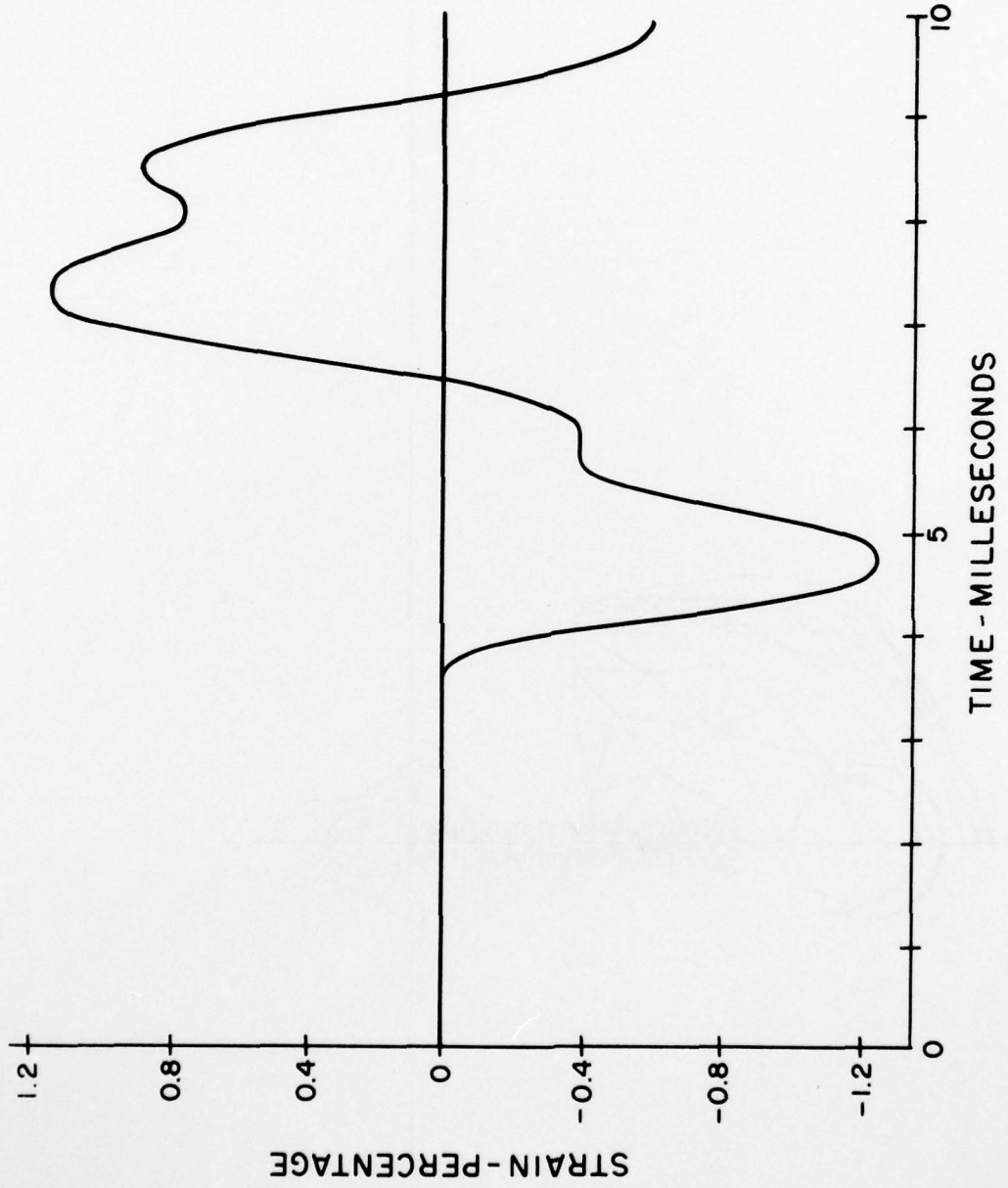

Figure 5.7 Time History of Strain in Vertical Brain-Spring Element

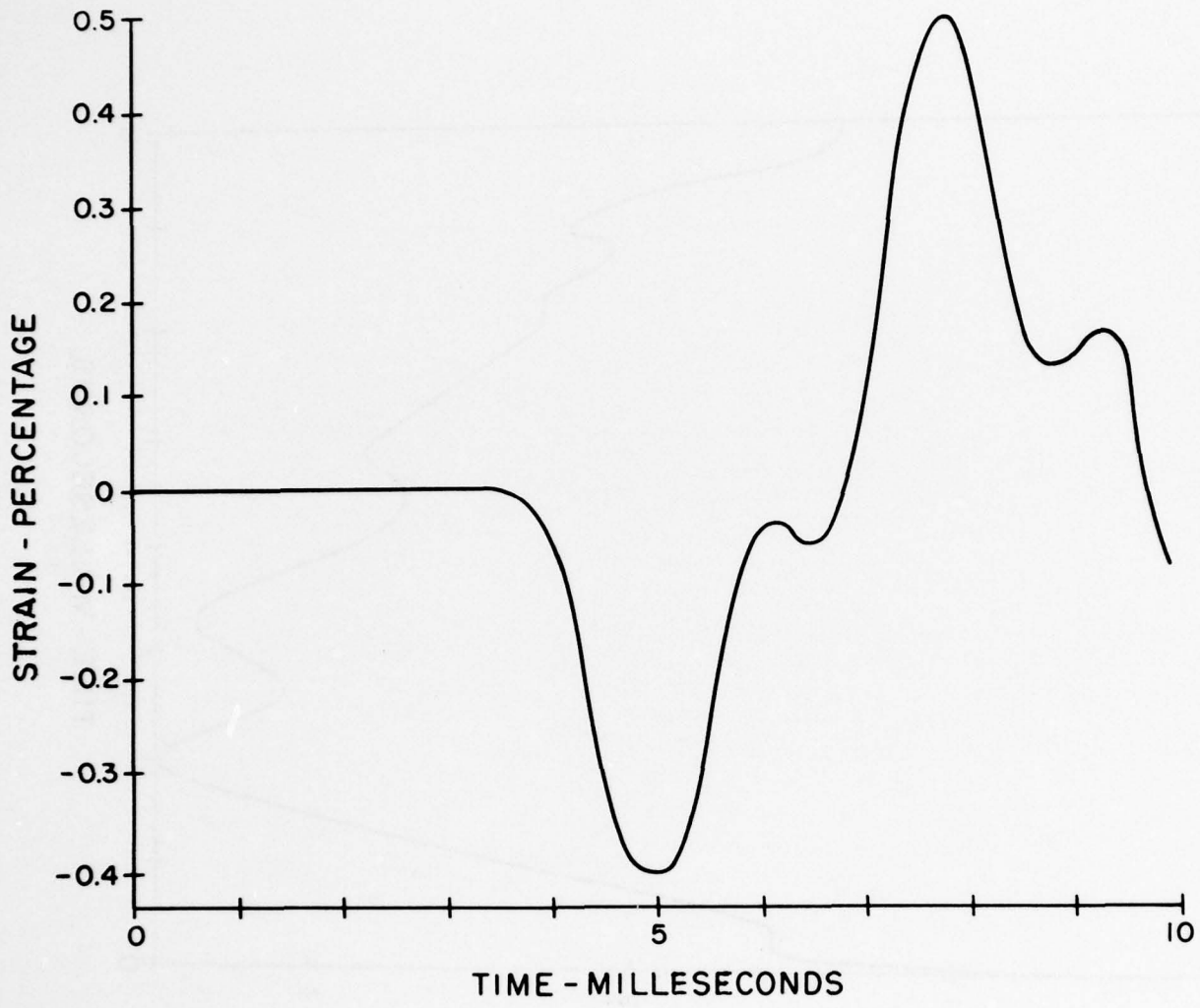

Figure 5.8 Time History of Strain in Anterior-Posterior Brain Spring Helmet

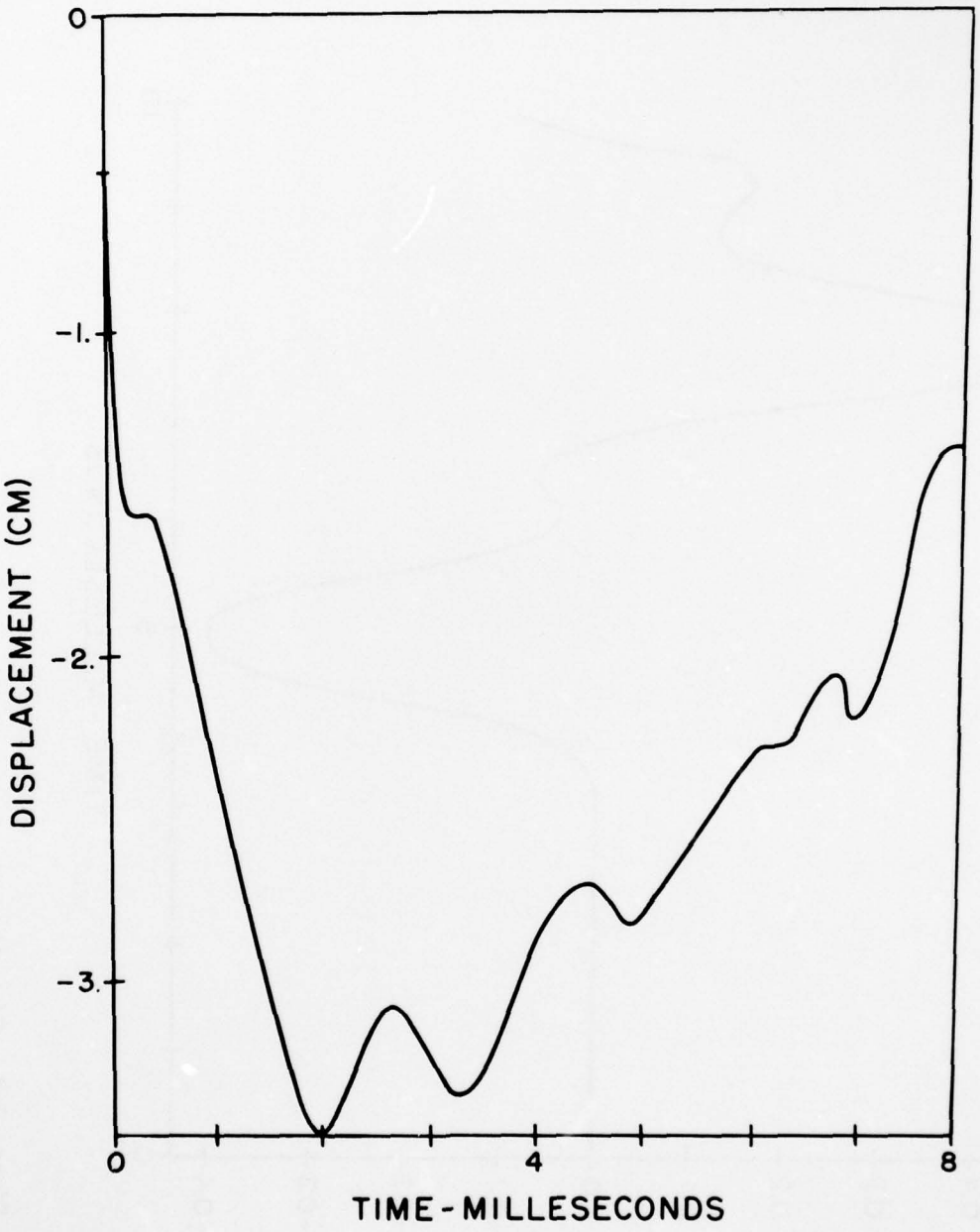

Figure 5.9 Displacement Time History of Node 88 (above anterior surface of pilot)

AD-A080 122 NORTHWESTERN UNIV EVANSTON IL DEPT OF CIVIL ENGINEERING F/G 6/5
COMPUTER SIMULATION OF CANOPY-PILOT RESPONSE TO BIRD-STRIKE.(U)
OCT 79 T BELYTSCHKO, E PRIVITZER, W WINDLE F33615-77-C-0529
UNCLASSIFIED AMRL -TR-79-20 NL

2 OF 2
AD
A080122

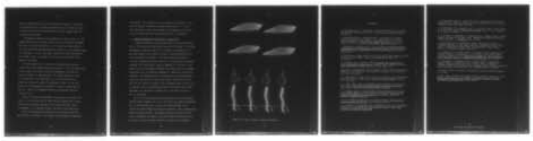

END
DATE
FILMED
3 - 80
DDC

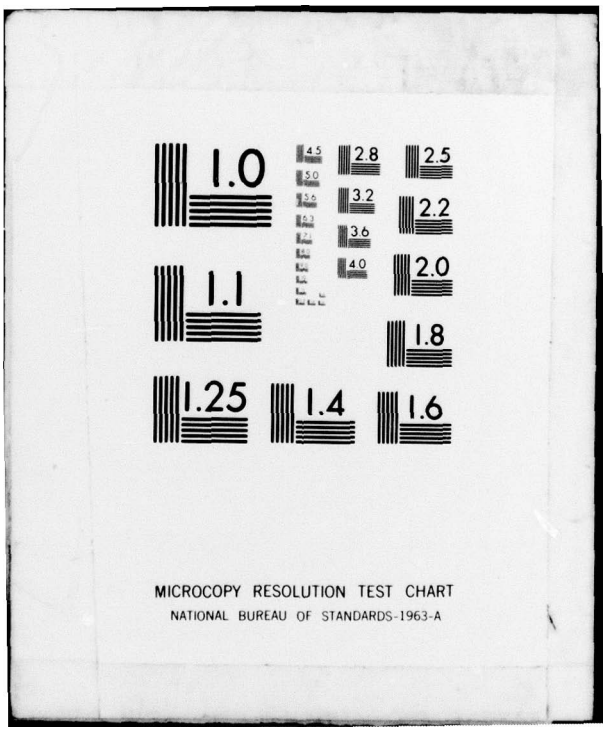
1.0
1.1
1.25
1.4
1.6
1.8
2.0
2.2
2.5
2.8
3.2
3.6
4.0
4.5
5.0
5.6
6.3
MICROCOPY RESOLUTION TEST CHART
NATIONAL BUREAU OF STANDARDS-1963-A

which is associated with a velocity and kinetic energy of 192.4 m/sec (374 knots) and 18.1 x 10^3 N-m, respectively, for a 0.98 kg (2.16 lbs) bird, and 103.5 m/sec (201 knots) and 9 x 10^3 N-m, respectively, for a 1.82 kg (4 lbs) bird.

The graphical display of this simulation is shown in Fig. 5.6 The maximum deflection at the impact point is 8 cm; which agrees reasonably well with the reported values at 4 to 12 cm for this energy level at the pilot station; the maximum deflection is about 5.5 cm, resulting barely in interference. In fact, the impact between the canopy and helmet is not evident in Fig. 5.6 because it occurs off the centerline in the middle of an element.

The time histories of a vertical (top) and anterior posterior (front) brain-spring element are given in Figs. 5.7 and 5.8, respectively. As can be seen, the initial strains are compressive, followed by a rebound of almost the same magnitude; the rebound appears to be due to the overshoot of the brain mass, for it occurs far before the helmet has a chance to contact the seatback; in fact, for the time duration of this simulation, no motion of the head is detectable in Fig. 5.6. However, the maximum strains are considerably below the tolerable level.

Figure 5.9 shows the displacement time history of node 88 of the canopy. It can be seen that the node deflects downward with a large velocity and then slowly rebounds to its initial position; this is a consequence of the nonlinear elastic law used in this simulation.

The fourth simulation was identical to the third but the pilot was initially 1 cm closer to the canopy, thus increasing the expected

interference. The character of this simulation was identical to the previous ones but the MSC was increased significantly. It can be seen from Table 5.2 that this decrease in interference is sufficient to raise the MSC above the value associated with no impairment.

5.3 Complete Simulation of Bird Strike - Canopy-Pilot.

A complete simulation of bird strike and pilot response was made with a 1.8 kg bird with a horizontal velocity of 250 m/sec. The canopy deformation is shown in Figure 5.10; it shows the progression of a wave-like pattern up the canopy but after the second indentation the bird ricochets off the canopy. The canopy strikes the helmet at 2.75 msec, imparting an initial velocity to the head with a horizontal component of 4.2 m/sec and a vertical component of -1.8 m/sec. This initial velocity is somewhat different than those found in the impulse simulations, for its horizontal component is larger than the vertical component. The simulation was not continued until the maximum strain occurred in the brain, but using these initial conditions it can be seen from the results of Chapter 3 that a maximum strain of about 1.35% is expected. This is substantially below the tolerance limit without impairment; the low value is probably due to the bird's failure to stay on the canopy.

The cost of this simulation was about $500.00 on the Northwestern CDC6600 system, compared to a cost of $75.00 for the impulse simulations. Part of the additional cost is due to the mesh refinement, which requires that more elements be used and in addition, that a substantially smaller time step be used. Furthermore, when the entire bird strike event is simulated, the impact to the pilot does not take place until much later, so that the total simulation time has to be increased.

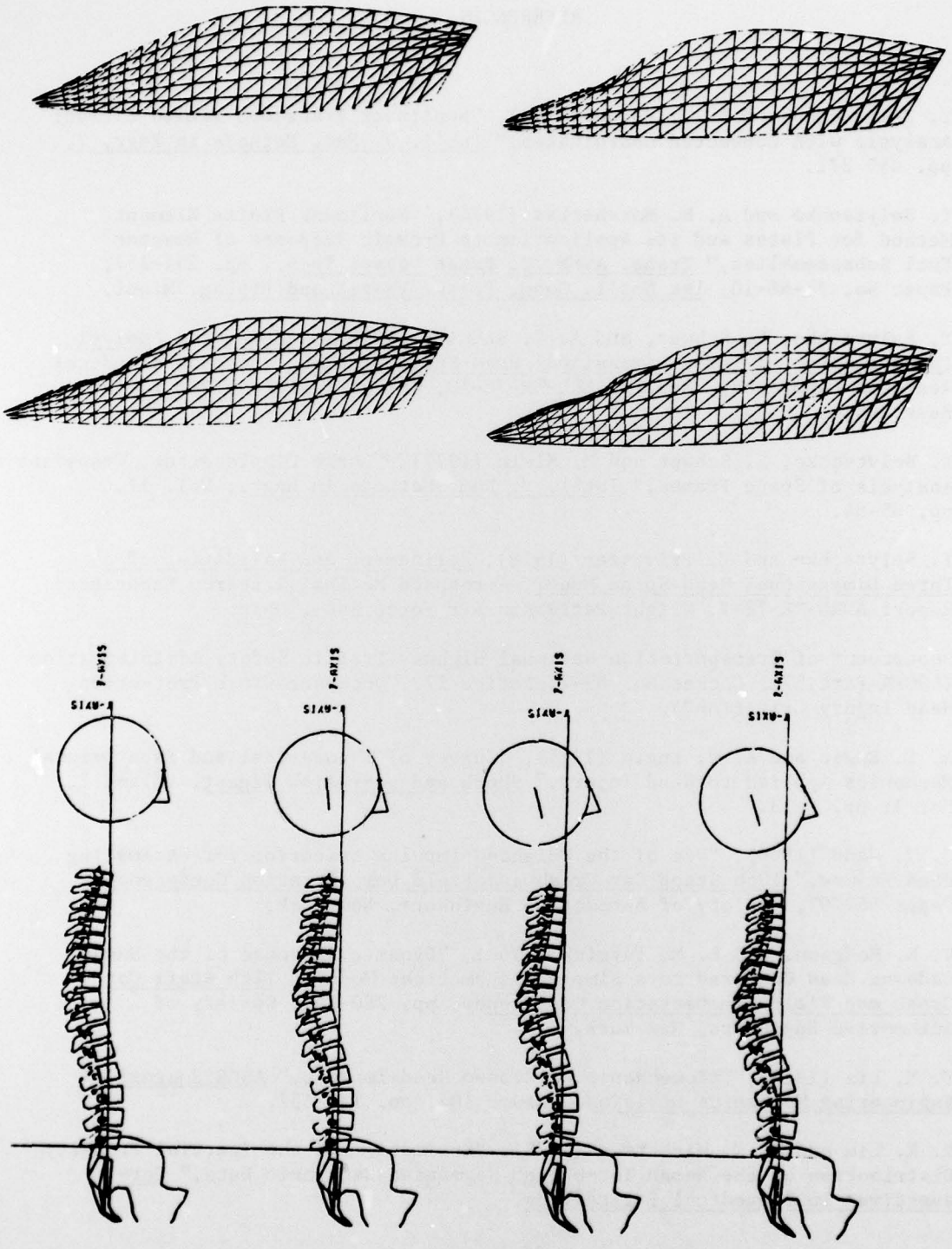

Figure 5.10 Graphic Display of Complete Simulation

REFERENCES

T. Belytschko and B. J. Hsieh (1973), "Nonlinear Transient Finite Element Analysis with Convected Coordinates," Int'l. J. Num. Methods in Engr. 7, pp. 255-271.

T. Belytschko and A. H. Marchertas (1974), "Nonlinear Finite Element Method for Plates and its Application to Dynamic Response of Reactor Fuel Subassemblies," Trans. ASME, J. Press Vessel Tech., pp. 251-257, Paper No. 74-NE-10, 1st Nat'l. Cong. Press. Vessel and Piping, Miami.

T. Belytschko, L. Schwer, and A. B. Schultz (1976), A Model for Analytic Investigation of Three-Dimensional Head-Spine Dynamics, Aerospace Medical Research Laboratory, Report AMRL-TR-76-10, Wright Patterson Air Force Base, Ohio.

T. Belytschko, L. Schwer and M. Klein (1977), "Large Displacement, Transient Analysis of Space Frames," Int'l. J. Num. Methods in Engr., Vol. 11, pp. 65-84.

T. Belytschko and E. Privitzer (1978), Refinement and Validation of a Three-Dimensional Head-Spine Model, Aerospace Medical Research Laboratory, Report AMRL-TR-78-7, Wright Patterson Air Force Base, Ohio.

Department of Transportation National Highway Traffic Safety Administration (49CFR Part 571, Docket No. 69-7; Notice 17, "Occupant Crash Protection Head Injury Criterion").

A. E. Engin and A. W. Engin (1975), "Survey of Theoretical and Experimental Mechanics Applied to Head Injury," Shock and Vibration Digest, Volume 7, No. 3, pp. 1-13.

C. W. Gadd (1966), "Use of the Weighted-Impulse Criterion for Estimating Head Injury," 10th Stapp Car Crash and Field Demonstration Conference, Paper 660793, Society of Automotive Engineers, New York.

V. R. Hodgson, and L. M. Patrick (1968), "Dynamic Response of the Human Cadaver Head Compared to a Simple Mathematical Model," 12th Staff Car Crash and Field Demonstration Conference, pp. 280-301, Society of Automotive Engineers, New York.

Y. K. Liu (1978), "Biomechanic of Closed Head Impacts," ASCE Journal of Engineering Mechanics Division, Volume 104, pp. 131-152.

Y. K. Liu and J. K. Wickstrom (1973), "Estimation of the Inertial Property Distribution of the Human Torso from Segmented Cadaveric Data," Perspectives in Biomedical Engineering.

A. H. Marchertas and T. B. Belytschko (1974), "Nonlinear Finite Element Formulation for Transient Analysis of Three-Dimensional Thin Structures," Argonne National Lab. Report ANL-8104.

J. H. McElhaney, R. L. Stalnaker, and V. L. Roberts (1973), "Biomechanical Aspects of Head Injury," Human Impact Response, edited by W. F. King and H. J. Mertz, pp. 85-112.

A. B. Schultz, T. Belytschko, T. Andriacchi and J. Galante (1973), "Analog Studies of Forces in the Human Spine: Mechanical Properties and Motion Segment Behavior," J. Biomech. 6, pp. 373-383.

A. Slattenschek and W. Tauffkirchen (1968), "Critical Evaluation of Assessment Methods for Head Impact Applied in Appraisal of Brain Injury Hazard, in Particular in Head Impact on Windshields," Paper 700426, Society of Automotive Engineers, New York.

L. J. Specker, N. S. Philips, and J. W. Brinkley (1978), "Application of Biodynamic Models to the Analysis of F-16 Canopy Bird Strike," AGARD Conference Preprint No. 253, Models and Analogues for the Evaluation of Human Biodynamic Response, Performance and Protection, Paris, France.

R. L. Stalnaker, J. McElhaney, and V. Roberts (1970), "A Mechanical Impedence Model for Head Injury due to Linear Impact," Symposium on Biodynamic Models and/or Applications, Aerospace Medical Research Laboratory, Wright-Patterson, Air Force Base, Ohio, AMRL-TR-71-29, pp. 905-932.

J. Versace, (1971), "A Review of the Severity Index for Technical Report," No. S-71-43.

C. Ward (1978), "A Head Injury Model," AGARD Conference Preprint No. 253, Models and Analogues for the Evaluation of Human Biodynamic Response, Performances, and Protection, Paris, France.

*U.S.Government Printing Office: 1979 — 657-084/322